

Morphological and Rotation Structures of Circumgalactic Mg II Gas in the EAGLE Simulation and the Dependence on Galaxy Properties

STEPHANIE H. HO,^{1,2} CRYSTAL L. MARTIN,³ AND JOOP SCHAYE⁴

¹*George P. and Cynthia Woods Mitchell Institute for Fundamental Physics and Astronomy, Texas A&M University, College Station, TX 77843-4242, USA*

²*Department of Physics and Astronomy, Texas A&M University, College Station, TX 77843-4242, USA*

³*Department of Physics, University of California, Santa Barbara, CA 93106, USA*

⁴*Leiden Observatory, Leiden University, P.O. Box 9513, 2300 RA, Leiden, The Netherlands*

ABSTRACT

Low-ionization-state Mg II gas has been extensively studied in quasar sightline observations to understand the cool, $\sim 10^4$ K gas in the circumgalactic medium. Motivated by recent observations showing that the Mg II gas around low-redshift galaxies has significant angular momentum, we use the high-resolution **EAGLE** cosmological simulation to analyze the morphological and rotation structures of the $z \approx 0.3$ circumgalactic Mg II gas and examine how they change with the host galaxy properties. Around star-forming galaxies, we find that the Mg II gas has an axisymmetric instead of a spherical distribution, and the axis of symmetry aligns with that of the Mg II gas rotation. A similar rotating structure is less commonly found in the small sample of simulated quiescent galaxies. We also examine how often Mg II gas around galaxies selected using a line-of-sight velocity cut includes gas physically outside of the virial radius (r_{vir}). For example, we show that at an impact parameter of 100 pkpc, a ± 500 km s⁻¹ velocity cut around galaxies with stellar masses of 10^9 - $10^{9.5}$ M_⊙ (10^{10} - $10^{10.5}$ M_⊙) selects Mg II gas beyond the virial radius 80% (6%) of the time. Because observers typically select Mg II gas around target galaxies using such a velocity cut, we discuss how this issue affects the study of circumgalactic Mg II gas properties, including the detection of corotation. While the corotating Mg II gas generally extends beyond $0.5r_{\text{vir}}$, the Mg II gas outside of the virial radius contaminates the corotation signal and makes observers less likely to conclude that gas at large impact parameters (e.g., $\gtrsim 0.25r_{\text{vir}}$) is corotating.

Keywords: Circumgalactic medium (1879), Extragalactic astronomy (506), Hydrodynamical simulations (767)

1. INTRODUCTION

The reservoir of baryons and metals surrounding galaxies regulates the interplay between gas accretion and feedback of galaxies and shapes the growth of galactic disks. Direct imaging of this circumgalactic medium (CGM) has proven challenging due to its low gas density. Observing the circumgalactic gas in absorption in the spectra of bright background sources circumvents this problem and has become a popular CGM observation approach. These sightline observations measure the absorption lines from various ions at different ionization states and then characterize the CGM properties, such

as the kinematics, radial distribution, chemical abundance, and phase structures (e.g., see [Tumlinson et al. 2017](#) for a review).

Circumgalactic absorption measurements have drawn attention to the inhomogeneous baryon distribution in the CGM. Sightlines near the galaxy major or minor axes often detect absorption systems with large equivalent widths and broad velocity ranges, whereas sightlines not aligning with either axis rarely detect these strong absorbers ([Bordoloi et al. 2011](#); [Bouché et al. 2012](#); [Kacprzak et al. 2012](#); [Nielsen et al. 2015](#); [Schroetter et al. 2019](#)). Such bimodality in spatial geometry is frequently observed for low-ionization-state (LIS) absorbers (e.g., Mg II), but it remains controversial whether the highly ionized O VI absorbers share the same characteristic ([Kacprzak et al. 2015](#)).

In addition to having a non-uniform distribution, the low-ionization circumgalactic gas does not move randomly and has significant angular momentum. Quasar sightline observations detected Doppler shifts of the LIS absorption sharing the same sign as the rotation of the galactic disk, indicating that the low-ionization CGM corotates with the galactic disks (Steidel et al. 2002; Kacprzak et al. 2010, 2011; Bouché et al. 2013, 2016; Ho et al. 2017; Martin et al. 2019; Zabl et al. 2019). The corotation may be unique to the LIS absorbers, as the highly ionized O^{+5} ion appears to be kinematically uniform and does not corotate with the disk (Nielsen et al. 2017; Kacprzak et al. 2019).

However, revealing the LIS absorbers corotating with the galactic disk does not uniquely identify the physical structure of the CGM. Martin et al. (2019) suggested that the corotating CGM around galaxies with stellar masses $\approx 10^{10} M_{\odot}$ is likely axisymmetric out to 70-kpc in radius. Their measurements showed a significant drop in Mg II covering factor for sightlines intersecting the disk plane at radii larger than 70 kpc, beyond which the correlation between the Mg II Doppler shift and the projected rotation velocity on the disk plane also weakened. While axisymmetry and rotation together suggest a rotating disk structure, a thin disk fails to explain the broad linewidth of the Mg II absorption (Steidel et al. 2002; Kacprzak et al. 2010, 2011; Ho et al. 2017). Instead, reproducing the linewidth requires a thick disk (Steidel et al. 2002) or a combination of the rotation on the extended disk plane and other components, such as outflow and tidal streams (Diamond-Stanic et al. 2016). Gas spiraling towards the inner disk presents another plausible scenario (Ho et al. 2017; Ho & Martin 2020). Alternatively, numerical simulations show other features that potentially explain the corotating circumgalactic gas observed, e.g., extended warped gas disks (Stewart et al. 2011, 2013), less “disky” rotating structures (El-Badry et al. 2018; Ho et al. 2019), accreting satellites (Shao et al. 2018), infalling streams from the cosmic web (Dekel et al. 2009; Danovich et al. 2015), and satellite winds (Hafen et al. 2018). In fact, decades of absorption-line studies have used the kinematic properties to identify the physical components associated with the absorbers (Lanzetta & Bowen 1992; Prochaska & Wolfe 1997; Charlton & Churchill 1998). But even now, we have yet to confirm the physical structures that correspond to individual components of the circumgalactic absorption.

The rotating LIS circumgalactic gas and the inhomogeneous distribution of circumgalactic baryons raise a seemingly simple question: what is the general structure of this low-ionization CGM, i.e., what does the

CGM “look” like? For individual objects, direct imaging of the CGM has only been possible for the difficult to interpret Lyman-alpha line, see Cantalupo et al. (2014), Borisova et al. (2016), and Cai et al. (2019) for radio quiet quasars and Wisotzki et al. (2016, 2018) and Leclercq et al. (2017) for Lyman-alpha emitters. Revealing the faint ionized CGM emission in other lines typically requires stacking many objects (Zhang et al. 2016, 2018; Guo et al. 2020), but the newly commissioned Keck Cosmic Web Imager (Morrissey et al. 2018) has made the imaging of the ionized CGM emission possible around individual systems; see the recent Mg II emission mappings by Burchett et al. (2020) of a starburst galaxy merger and Chisholm et al. (2020) of a Lyman Continuum emitter. On the other hand, although sightlines around individual typical galaxies probe the CGM and reveal its properties, the major limitation of this technique is the small number of sightlines per galaxy. Most CGM surveys stack single-sightline observations to characterize the properties of the average CGM (Rakic et al. 2012; Tumlinson et al. 2013; Werk et al. 2013; Turner et al. 2014; Borthakur et al. 2015, 2016; Heckman et al. 2017; Chen et al. 2018; Rubin et al. 2018a; Martin et al. 2019). Only under rare circumstances do multi-sightline observations become possible, such as with gravitationally lensed quasars (Chen et al. 2014; Zahedy et al. 2016; Rubin et al. 2018b; Kulkarni et al. 2019) and galaxies (Lopez et al. 2018, 2019), or with multiple bright sources fortuitously located behind the target galaxies at small projected angular separations (e.g., Muzahid 2014; Bowen et al. 2016; Péroux et al. 2018; Zabl et al. 2020). Hence, CGM tomography remains challenging until the advent of next generation telescopes.

The uncertainty in associating the absorption system with the host galaxy presents another challenge for observational analysis of the CGM. Typically, observers associate the absorption system with a galaxy at small projected separation with the sightline and at comparable redshift, i.e., with small line-of-sight (LOS) velocity separation. However, because absorption-line measurements do not reveal where the absorbing gas lies along the sightline, the gas potentially resides beyond the CGM of the assumed host. In addition, many faint galaxies may remain undetected. These uncertainties lead to possible errors in determining the circumgalactic gas properties, especially when individual systems cannot be closely examined in surveys with thousands of galaxy-absorber pairs (e.g., Bordoloi et al. 2011; Lan et al. 2014; Zhu et al. 2014; Lan & Mo 2018).

In contrast to observational studies, hydrodynamical simulations can directly “image” the low-density CGM and reveal the circumgalactic gas distribution and kine-

matics. These simulations generally reproduced the radial distribution of the column density of LIS ions (Ford et al. 2014, 2016; Liang et al. 2016; Oppenheimer et al. 2018a; Nelson et al. 2020) but underpredicted that of the highly ionized O^{+5} ion (Hummels et al. 2013; Oppenheimer et al. 2016; Gutcke et al. 2017; Suresh et al. 2017), an issue potentially resolved by black hole feedback (Nelson et al. 2018) or fossil AGN proximity zones (Oppenheimer & Schaye 2013; Oppenheimer et al. 2018b). Simulations also found rotating gas structures around $z \approx 0$ galaxies extended out to tens or ~ 100 kpc (El-Badry et al. 2018; Ho et al. 2019), where the angular momentum vector of the circumgalactic gas aligned with that of the stellar disk (DeFelippis et al. 2020; Huscher et al. 2020). The morphology of the extended gas depends on the galaxy properties and the feedback physics (e.g., van de Voort & Schaye 2012; Kauffmann et al. 2016, 2019). Nevertheless, these results show that the CGM has a rotation component, agreeing qualitatively with the picture of the low-ionization CGM suggested by quasar sightline observations.

This paper studies the low-ionization circumgalactic gas using the high-resolution EAGLE simulation (Crain et al. 2015; Schaye et al. 2015). EAGLE has proven capable of broadly reproducing many galaxy observables, including the galaxy stellar mass function (Schaye et al. 2015), the evolution of galaxy masses (Furlong et al. 2015), sizes (Furlong et al. 2017), colors (Trayford et al. 2015, 2017), and gas contents (Lagos et al. 2015; Bahé et al. 2016; Crain et al. 2017). The simulation was not calibrated to match observational measurements of the intergalactic medium (IGM) nor the CGM; it was calibrated to match the present-day galaxy stellar mass function, the sizes of disk galaxies, and the amplitude of the galaxy-central black hole mass relation. Therefore, EAGLE provides a testbed for understanding and testing against the results from CGM observations. EAGLE shows broad agreements with absorption-line statistics for H I (Rahmati et al. 2015) and metal ions (Rahmati et al. 2016; Turner et al. 2016, 2017; Oppenheimer et al. 2018a). In particular, Oppenheimer et al. (2018a) demonstrated that EAGLE reproduces the commonly observed anticorrelation between covering fraction of low ions (e.g., Si II, Si III, C II) and impact parameter. The cumulative distribution functions of the simulated column densities of low ions match with those from the COS-Halos survey (Tumlinson et al. 2013), an HST/COS program that characterizes the CGM of $z \approx 0.2$, $\sim L^*$ galaxies through quasar sightline observations. The ion ratios and pressures of the low-ion metal clumps in EAGLE also agree with that deduced from the COS-Halos sample. Although EAGLE under-

produces the O^{+5} ion, it reproduces the observed O VI bimodality around blue and red galaxies (Oppenheimer et al. 2016). Not only does EAGLE provide insights on interpreting CGM observations and on understanding the origin and distribution of the multiphase gas (e.g., Stevens et al. 2017; Correa et al. 2018a,b; Oppenheimer et al. 2018b; Oppenheimer 2018; Ho et al. 2019; Huscher et al. 2020, etc.), but EAGLE also makes predictions for CGM/IGM observations with future instruments, e.g., the column density and equivalent width distribution of O VII, O VIII, and Ne IX absorption systems in X-ray observations (Wijers et al. 2019, 2020).

This study examines the LIS Mg II gas in the low-redshift CGM and focuses on the morphology and the rotation structure. We also investigate how often selecting the Mg II gas around galaxies using a LOS velocity cut actually detects Mg II outside of the halo virial radius r_{vir} ; we refer to this Mg II outside of r_{vir} as being “mis-assigned”, which creates the issue of “Mg II host galaxy mis-assignment”. We examine how this issue affects circumgalactic gas detection and measurement in sightline observations. We note that we use the term “mis-assigned” simply to mean outside of r_{vir} and does not necessarily mean outside of the CGM, because the CGM possibly extends beyond r_{vir} (Shull 2014). We focus on Mg II in this paper, because Mg II is the most commonly studied ion in low-redshift CGM observations and also because of the recent results on the Mg II rotation kinematics (Ho et al. 2017; Martin et al. 2019). We present this paper as follows. Section 2 describes the EAGLE galaxy selection. Section 3 examines how the Mg II gas outside of r_{vir} affects the detection of Mg II gas with impact parameters smaller than r_{vir} and addresses the significance of host galaxy mis-assignments in observations. In Section 4, we analyze the morphology and the rotation structure of the Mg II gas around galaxies and examine how they vary across different galaxy populations. We also explore how the mis-assigned Mg II gas affects the Mg II rotation analyses. In Section 5, we discuss the implication of our results and relate them to recent observation and simulation analyses. Finally, we conclude in Section 6. Throughout this paper, we use the flat Λ CDM cosmology with $(\Omega_m, \Omega_\Lambda, h) = (0.307, 0.693, 0.6777)$ adopted by EAGLE from Planck Collaboration et al. (2014).

2. THE EAGLE SIMULATION AND GALAXY SELECTION

2.1. Simulation Overview

The EAGLE simulation suite consists of a large number of cosmological hydrodynamic simulations with different cosmological volumes, resolutions, and subgrid physics

Table 1. Characteristics of the Recal-L0025N0752 simulation used in this paper.

Simulation Property		Value
(1)	Box size L (cMpc)	25
(2)	Number of particles N	752 ³
(3)	Initial baryonic particle mass m_g (M_\odot)	2.26×10^5
(4)	Dark matter particle mass m_{dm} (M_\odot)	1.21×10^6
(5)	Gravitational softening length ϵ_{com} (ckpc)	1.33
(6)	Maximum softening length ϵ_{prop} (pkpc)	0.35

NOTE— (1) Comoving box size. (2) Number of dark matter particles (initially there is an equal number of baryonic particles). (3) Initial baryonic particle mass. (4) Dark matter particle mass. (5) Comoving Plummer-equivalent gravitational softening length. (6) Maximum proper softening length.

(Schaye et al. 2015; Crain et al. 2015; McAlpine et al. 2016). *EAGLE* was run using a modified version of the N -Body Tree-PM smoothed particle hydrodynamics (SPH) code *GADGET-3* (last described in Springel 2005) with a new hydrodynamics solver (Schaller et al. 2015). State-of-the-art subgrid models were implemented to capture unresolved physics, including radiative cooling and photoheating, star formation, stellar evolution and enrichment, stellar feedback, and active galactic nuclei feedback and black hole growth. Schaye et al. (2015) introduced a reference model; the parameters of the subgrid models for energy feedback from stars and accreting black holes were calibrated to reproduce the galaxy stellar mass function at $z \approx 0$ and the sizes of present-day disk galaxies.

EAGLE defines galaxies as gravitationally bound substructures identified by the SUBFIND algorithm (Springel et al. 2001; Dolag et al. 2009). In brief, the friends-of-friends (FoF) algorithm places dark matter particles into the same group if the particle separation is below 0.2 times the average particle separation. Baryons are associated with the same FoF halo (if it exists) as their closest dark matter particle. In each FoF halo, SUBFIND defines self-bound overdensities of particles as subhalos; each subhalo represents a galaxy. The central galaxy is defined as the subhalo with the particle at the lowest gravitational potential, and the remaining subhalos are classified as satellite galaxies.

In this study, we focus on the simulation Recal-L0025N0752,¹ which has a box size of 25 cMpc and

¹ The “Recal” model was calibrated to the same $z \sim 0$ galaxy properties as the reference model, but small changes were made to the stellar and AGN feedback subgrid parameters as a consequence of the higher resolution compared to the default resolution runs.

Table 2. Galaxy count by stellar mass and star-forming vs. quiescent. Only central galaxies are included.

	Star-forming	Quiescent
$9.0 \leq \log(M_\star/M_\odot) < 9.5$	57	6
$9.5 \leq \log(M_\star/M_\odot) < 10.0$	46	2
$10.0 \leq \log(M_\star/M_\odot) < 10.5$	35	9
$10.5 \leq \log(M_\star/M_\odot) < 11.0$	6	7
Total Number of Galaxies	144	24

8 (2) times better mass (spatial) resolution than the *EAGLE* default intermediate resolution runs, e.g., Ref-L0100N1504. We summarize the simulation parameters in Table 1. We use the particle data output² and focus on galaxies at a single “snapshot” of $z = 0.271$; this redshift is comparable to the galaxy redshifts in recent quasar absorption-line studies that measure the CGM kinematics of low-redshift galaxies (e.g., Ho et al. 2017; Martin et al. 2019). The Hubble parameter at this redshift is $H(z = 0.271) = 78.0 \text{ km s}^{-1} \text{ Mpc}^{-1}$, and the box size of 25 cMpc corresponds to 1533 km s^{-1} . Because *EAGLE* applies periodic boundary conditions, the maximum LOS separation is half of the 25 cMpc box size, i.e., 12.5 cMpc, which corresponds to a velocity difference of 767 km s^{-1} (physical) at $z = 0.271$.

2.2. Galaxy Selection from the *EAGLE* Simulation

We select central galaxies with stellar masses (M_\star) between 10^9 to $10^{11} M_\odot$. The stellar mass is defined as the total mass of the star particles associated with the subhalo and located within a 30-pkpc radius (in 3D) from the galaxy center (Schaye et al. 2015). The galaxy star formation rate (SFR) is defined using the same 3D aperture. Figure 1 shows the selected galaxies on the SFR– M_\star plane, and the color of each point represents the galaxy specific SFR (sSFR). The gray dashed line separates star-forming galaxies from quiescent galaxies; the line is a redshift-dependent relation fitted from $\sim 120,000$ galaxies with spectroscopic redshifts from the PRISM Multi-object Survey (Moustakas et al. 2013). Our sample consists of mainly star-forming galaxies; the 168 central galaxies include 144 star-forming and 24 quiescent galaxies (Table 2). The M_\star and the sSFR distributions of the galaxies are shown in the histograms.

The selected central galaxies span a halo virial mass range between $10^{10.6}$ and $10^{13.2} M_\odot$ with a median of

² Particle data from snapshots can be downloaded from <http://icc.dur.ac.uk/Eagle/database.php>

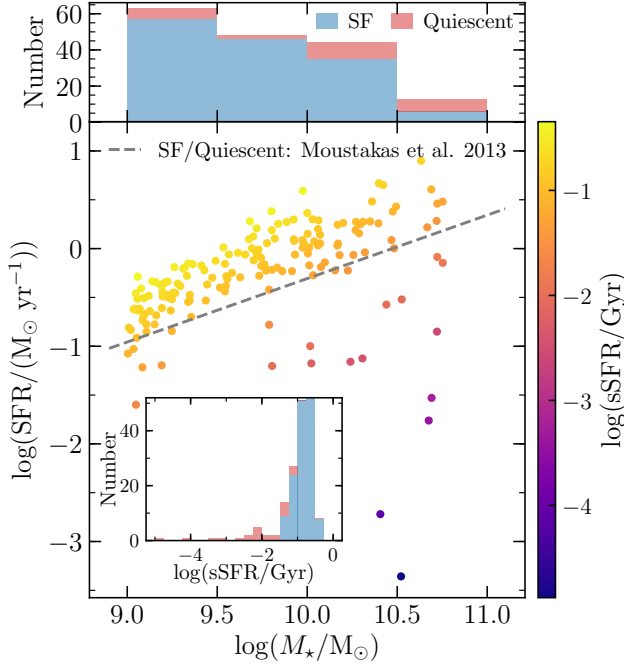


Figure 1. Central galaxies on the SFR– M_* plane. Each point is colored by the galaxy sSFR ($= \text{SFR}/M_*$). The gray dashed line divides the galaxies into either star-forming or quiescent if the galaxies lie above or below the line, respectively (Moustakas et al. 2013). Among the 168 central galaxies with stellar masses between 10^9 and 10^{11} M_\odot , the sample consists of 144 star-forming and 24 quiescent galaxies. The histograms at the top and in the inset show the distributions of M_* and sSFR, respectively.

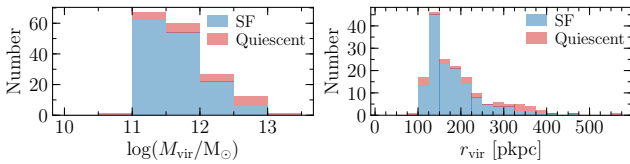


Figure 2. Distributions of halo virial mass M_{vir} and virial radius r_{vir} of selected central galaxies. The virial mass (left) ranges from $10^{10.6}$ to $10^{13.2} \text{ M}_\odot$, and the median is $10^{11.6} \text{ M}_\odot$. The median virial radius is 170 pkpc and ranges from 78 pkpc to 568 pkpc (right).

$10^{11.6} \text{ M}_\odot$ (left panel of Figure 2). We define the virial radius r_{vir} as the radius enclosing an average density of $\Delta_{\text{vir}}\rho_c(z)$, where $\rho_c(z)$ represents the critical density at redshift z , and the overdensity Δ_{vir} follows the top-hat spherical collapse calculation in Bryan & Norman (1998). For our galaxy sample at $z = 0.271$, the median virial radius is 170 pkpc, and the individual virial radii vary from 78 to 568 pkpc (right panel).

For each galaxy, we define its orientation using the net specific angular momentum vector of the star par-

ticles \mathbf{j}_* within the 30-pkpc aperture. The plane that intersects the galaxy center and is normal to the angular momentum vector defines the disk midplane. We use this orientation to define how we project galaxies onto 2D planes while observing the galaxies at fixed inclination angles.

2.3. Two-dimensional Projection Maps

We project galaxies either along fixed simulation box axes (Section 3) or at fixed galaxy inclination angles (Section 4). Then, we produce the Mg II column density maps and the Mg II-weighted LOS velocity maps. The calculation of the ionic column density requires the tracked element abundance and the ion fraction, which is the number of atoms in each ionization state relative to the total number of atoms of the element in the gas phase. We obtain the ion fraction (f_{ion}) using the tables from the fiducial model presented in Ploeckinger & Schaye (2020), UVB_dust1.CR1.G1.shield1.³ They used CLOUDY v17.01 (Ferland et al. 2017) to tabulate the properties of gas (e.g., cooling and heating rates, ion fraction, etc.) for a wide range of gas density, temperature, metallicity, and redshift. In this fiducial model, the calculations assume ionization equilibrium, and the gas is exposed to the redshift-dependent UV/X-ray background by Faucher-Giguère (2020)⁴, the interstellar radiation field, and cosmic rays. The model also accounts for the depletion of metals onto dust grains, tabulated as the number fraction of atoms depleted (f_{dust}) for each element. The effect of self-shielding is included; the radiation at the center of a gas cloud is attenuated by its dust and gas and can be self-shielded from photoionizing radiation, leaving the cloud cold and neutral at the inside but ionized at the outside. This is modeled by passing the incident radiation field through a gas shielding column, which is set to half of the local Jeans column density; the latter is the typical scale for self-gravitating gas. Using the f_{ion} and f_{dust} tables, we obtain the ion balances for each SPH particle and calculate the number of ions through a column in the simulation box (see Section 2 of Wijers et al. 2019 for details of creating column density maps from SPH particles). Note that the ion fraction will differ somewhat from that used to compute cooling rates during the simulation, since EAGLE used an older version of CLOUDY, a different UV back-

³ The hdf5 tables are publicly available on <http://radcool.strw.leidenuniv.nl> and <https://www.sylviaploeckinger.com/radcool>.

⁴ Ploeckinger & Schaye (2020) modified the $z > 3$ UV/X-ray background in Faucher-Giguère (2020) to make the treatment of attenuation before H I and He II reionization more self-consistent (see their Appendix B). This modification is irrelevant to this work at $z = 0.271$.

ground model and did not include self-shielding. We do not expect this to be important, however, because magnesium is not an important coolant (Wiersma et al. 2009).

In addition, due to the lack of resolution to resolve the interstellar gas phase at $\ll 10^4$ K, EAGLE imposes a temperature floor, such that the effective equation of state prevents artificial Jeans fragmentation (Schaye & Dalla Vecchia 2008). Therefore, before calculating the Mg^+ ion fraction, we change the temperature of star-forming gas to 10^4 K, which is the typical temperature of the warm-neutral interstellar medium (ISM).

We select the Mg II gas using two separate ways to make the projection maps. The first method is to include only the gas within r_{vir} . This method excludes the Mg II gas physically separated from the target galaxies but appearing to be closeby on the projection maps. As for the second method, we include the Mg II gas within a certain LOS velocity separation $|\Delta v_{\text{LOS}}|$ from the systemic velocity of the target galaxy. We adopt $|\Delta v_{\text{LOS}}| = 500 \text{ km s}^{-1}$, which is commonly used in observational studies to associate absorption systems with host galaxies (e.g., Chen et al. 2010, 2018; Werk et al. 2013).

We produce the maps of the Mg II column density and the Mg II-weighted LOS velocity using the selected Mg II gas. Each pixel on the column density maps shows the column summed along the pathlength enclosed by r_{vir} or the $|\Delta v_{\text{LOS}}|$ window, and the LOS velocity maps show the projected velocity weighted by the column density of the enclosed gas. Each pixel has an area of either $(1.25 \text{ pkpc})^2$ or $(0.005 r_{\text{vir}})^2$. While varying the pixel size changes the column density at the pixel, e.g., a coarser pixel smooths out the high column density region, the conclusions of our analyses remain unchanged if we double or halve the pixel size (see also the discussion in the Appendix of Wijers et al. 2019). While we adopt the fiducial model in Ploeckinger & Schaye (2020) throughout this paper, we have explored using their other models to understand how interstellar radiation and cosmic rays, self-shielding, and dust depletion affect the CGM Mg II column density. We find that the effect of dust depletion is tiny and changes the Mg II column density by no more than 0.02 dex. Turning off the interstellar radiation and cosmic rays (model UVB_dust1.CR0.G0_shield1) increases the Mg II column density typically by 0.01 to 0.02 dex; this small change suggests that most of the circumgalactic Mg II does not come from ISM densities. Lastly, comparing the results from the fiducial model to that of without self-shielding (model UVB_dust1.CR1.G1_shield0) shows that self-shielding boosts the Mg II column den-

sity typically by 0.1 to 0.3 dex. This suggests that including self-shielding is important for analyzing Mg II gas, especially because Mg II traces higher densities compared to other commonly observed low ions, such as Si II and C II.⁵

To resemble the “detection limit” of Mg II absorption in CGM observations, we impose a Mg II detection limit of $N_{\text{MgII}} = 10^{11.5} \text{ cm}^{-2}$. This limit is comparable to the typical observational limit of $\sim 10^{12} \text{ cm}^{-2}$ (e.g., Werk et al. 2013; Martin et al. 2019), and we also take into account the potentially ≈ 0.3 dex too low magnesium nucleosynthetic yields in EAGLE (Segers et al. 2016). Hence, we consider the Mg II gas as “detectable” only if its column density exceeds the detection limit of $N_{\text{MgII}} = 10^{11.5} \text{ cm}^{-2}$.

3. Mg II HOST GALAXY MIS-ASSIGNMENT

Observers typically associate a Mg II absorption system with a galaxy host close to the sightline (typically $< 300 \text{ kpc}$, e.g., Churchill et al. 1996; Kacprzak et al. 2007; Nielsen et al. 2013b) and with redshift similar to that of the absorption. The latter is typically defined using a LOS velocity window $|\Delta v_{\text{LOS}}|$ centered at the galaxy systemic redshift (e.g., 500 km s^{-1} , Chen et al. 2010, 2018; Werk et al. 2013).⁶ However, observations cannot determine where the absorbing gas lies along the sightline; the absorbing gas potentially lies beyond the virial radius of the galaxy but satisfies the LOS velocity selection criterion, i.e., the Mg II gas is mis-assigned. In this section, we address this issue of Mg II host galaxy mis-assignment and explore how this problem varies across galaxies with different characteristics.

3.1. Detecting Mg II Gas Mis-assigned to the Target Galaxies

For each galaxy, we integrate the column along the z -axis of the simulation box and produce two sets of Mg II column density maps. The first map includes only the Mg II gas within r_{vir} , whereas the second map includes the Mg II gas within $|\Delta v_{\text{LOS}}| = 500 \text{ km s}^{-1}$ from the galaxy systemic velocity. We name these two columns the r_{vir} column and the $|\Delta v_{\text{LOS}}|$ column, respectively, and calculate their column density difference, i.e., $\log \Delta N_{\text{MgII}} = \log(N_{\text{MgII}, |\Delta v|} - N_{\text{MgII}, r_{\text{vir}}})$. This difference represents the column density of the Mg II gas

⁵ Mg II traces gas with $n_{\text{H}} \gtrsim 10^{-2} \text{ cm}^{-2}$, whereas Si II and C II trace $n_{\text{H}} \gtrsim 10^{-3} \text{ cm}^{-2}$ and $n_{\text{H}} \gtrsim 10^{-4} \text{ cm}^{-2}$ gas, respectively (e.g., Tumlinson et al. 2017).

⁶ In Chen et al. (2010) and Chen et al. (2018), even though they used a LOS velocity search window of $\pm 500 \text{ km s}^{-1}$, over 90% of the absorbers are found to be within 300 km s^{-1} of the galaxies.

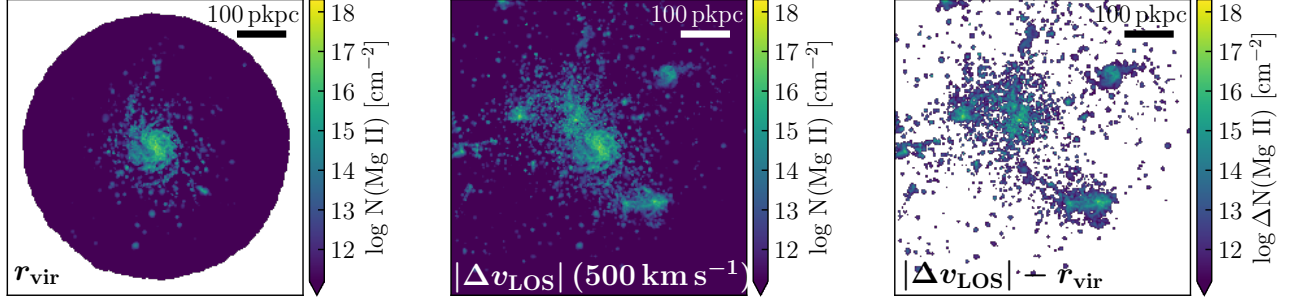


Figure 3. Example of mis-assigning Mg II gas structures to a star-forming galaxy with $\log(M_*/M_\odot) = 10.4$. (Left) The Mg II gas within r_{vir} . The region outside of r_{vir} is shown in white. (Middle) The Mg II gas within the LOS velocity window of $\pm 500 \text{ km s}^{-1}$ from the galaxy systemic velocity. (Right) Column density difference between the r_{vir} and the $|\Delta v_{\text{LOS}}|$ columns, i.e., $\log(N_{\text{MgII},|\Delta v|} - N_{\text{MgII},r_{\text{vir}}})$. Below the detection limit of $10^{11.5} \text{ cm}^{-2}$, the excess Mg II column density is not “detectable” and is shown in white. The x and y axes of the maps align with those of the simulation box, and the column density is integrated along the z -axis. All maps are $600 \text{ pkpc} \times 600 \text{ pkpc}^2$.

outside of r_{vir} but would have erroneously associated with the galaxy if we use the $|\Delta v_{\text{LOS}}|$ window to identify the Mg II host. This mis-assigned Mg II gas is “detectable” if its column density ($\log \Delta N_{\text{MgII}}$) exceeds the Mg II detection limit.

The column density maps in Figure 3 illustrate an example of detecting the mis-assigned Mg II gas. When we include the Mg II gas within the $\pm 500 \text{ km s}^{-1}$ LOS velocity window (middle), the map shows additional regions with high Mg II column density compared to that of the Mg II gas within r_{vir} (left). The column densities of these extra Mg II structures exceed the Mg II detection limit (right), and sightline observations would have associated these structures with the target galaxy.

3.2. The Significance of Detecting Mis-assigned Mg II Gas

We examine how the Mg II gas outside of r_{vir} affects the Mg II detection rate around target galaxies. For individual galaxies, we produce the maps of the column density difference ($\log \Delta N_{\text{MgII}}$) between the r_{vir} and the $|\Delta v_{\text{LOS}}|$ columns as in Figure 3. We flag the pixels as detecting mis-assigned Mg II gas if $\log \Delta N_{\text{MgII}}$ exceeds the Mg II detection limit.⁷ Then, we stack these maps for galaxies in different stellar mass bins. At each pixel of individual stacks, we calculate two quantities: (1) the number of galaxies flagged, and (2) the number of galaxies with the $|\Delta v_{\text{LOS}}|$ column exceeding the Mg II detection limit, i.e., the Mg II gas is “detectable” in the

Table 3. Fitted parameters for the Mg II mis-assignment fraction represented by $f_{\text{MgII},\text{mis}}(b) = 1/(1 + e^{-\beta(b-b_{1/2})})$.

Galaxy Stellar Mass	β (pkpc $^{-1}$)	$b_{1/2}$ (pkpc)
$9.0 \leq \log(M_*/M_\odot) < 9.5$	0.0536 ± 0.0024	78 ± 1
$9.5 \leq \log(M_*/M_\odot) < 10.0$	0.0393 ± 0.0011	148 ± 1
$10.0 \leq \log(M_*/M_\odot) < 10.5$	0.0254 ± 0.0004	214 ± 1
$10.5 \leq \log(M_*/M_\odot) < 11.0$	0.0131 ± 0.0005	321 ± 3

first place. We bin the pixels by every 10 pkpc in impact parameter b , which is the projected separation between individual pixels and the galaxy center. Then, we divide the two quantities (after binning) to obtain the Mg II mis-assignment fraction $f_{\text{MgII},\text{mis}}$. In other words, we are asking the question: for a LOS with a detectable amount of Mg II at $|\Delta v_{\text{LOS}}| \leq 500 \text{ km s}^{-1}$, what is the probability that a detectable fraction of this Mg II resides beyond r_{vir} ?

Figure 4 plots Mg II mis-assignment fraction, $f_{\text{MgII},\text{mis}}$, as a function of impact parameter b and shows how this changes with galaxy stellar mass. The four colors, from dark to light, show the results from the stacks of galaxies with increasing stellar masses. Clearly, the Mg II mis-assignment fraction increases with impact parameter and approaches 1. The latter is expected; when $b > r_{\text{vir}}$ for individual galaxies, the column no longer intersects any region within r_{vir} (vertical lines show the medians), and any Mg II gas detected must be outside of r_{vir} .⁸

⁷ This $\log \Delta N_{\text{MgII}}$ calculation implicitly assumes that the Mg II gas within the r_{vir} column is also within the $|\Delta v_{\text{LOS}}| = 500 \text{ km s}^{-1}$ column. This is a reasonable assumption; absorption-line studies showed that the circumgalactic gas is bound to the galaxies (Werk et al. 2013). We analyzed the simulation and also found that this assumption has negligible effects on the Mg II mis-assignment fractions we are calculating.

⁸ The $f_{\text{MgII},\text{mis}}$ does not always reach 1 at the vertical lines of Figure 4, because the vertical lines only show the median r_{vir} of the galaxies in each stack.

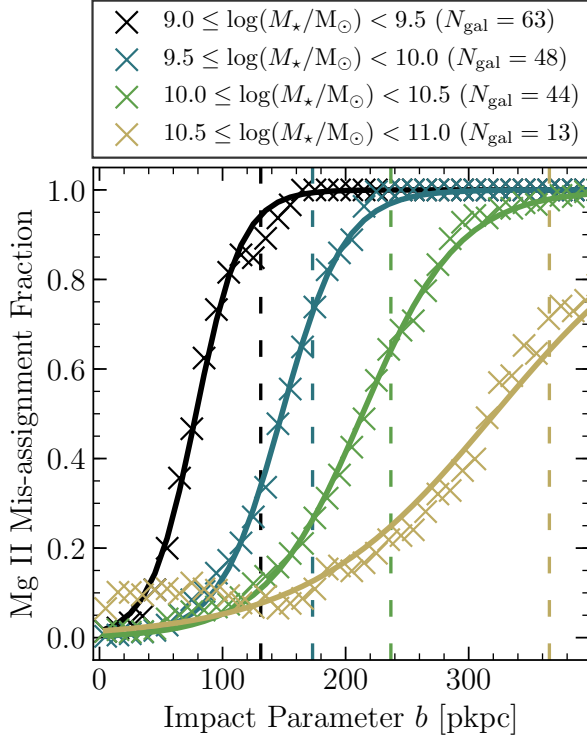


Figure 4. Variations of Mg II mis-assignment fractions with impact parameter and galaxy stellar mass. The mis-assignment fraction $f_{\text{MgII},\text{mis}}$ measures how likely it is that a detectable amount of Mg II gas lies outside of r_{vir} but is selected by the $|\Delta v_{\text{LOS}}| = 500 \text{ km s}^{-1}$ window, i.e., the Mg II gas is mis-assigned to the target galaxy. Each color represents the result from each stack of galaxies in each stellar mass bin. The vertical lines show the median r_{vir} of the corresponding galaxy stacks. Each curve shows the analytic fit to $f_{\text{MgII},\text{mis}}$ for each galaxy stack.

We fit an analytical function to describe the increase of the Mg II mis-assignment fraction with impact parameter. We adopt the functional form of $f_{\text{MgII},\text{mis}}(b) = 1/(1 + e^{-\beta(b-b_{1/2})})$, where β describes the steepness of the rise, and $b_{1/2}$ represents the impact parameter where $f_{\text{MgII},\text{mis}} = 0.5$. The solid curves in Figure 4 show the fits, and Table 3 lists the best-fit β and $b_{1/2}$ for the stacks of galaxies with different stellar masses. For example, $b_{1/2}$ is only 78 pkpc for galaxies at the lowest stellar mass bin. This means that 50% of the time, sightline observations with impact parameters of ≈ 100 pkpc would mis-assign the galaxy host of the “detected” Mg II gas. The best-fit $b_{1/2}$ (β) increases (decreases) with increasing galaxy stellar mass. Hence, at a fixed impact parameter, the detected Mg II gas around a less massive galaxy is more likely to be mis-assigned.

Our calculated Mg II mis-assignment fraction represents a conservative estimate. As a result of the EAGLE periodic boundary conditions, the maximum LOS separation

in the 25 cMpc box at $z = 0.271$ is 767 km s^{-1} (see Section 2.1). Because this is not significantly larger than our $|\Delta v_{\text{LOS}}| \leq 500 \text{ km s}^{-1}$ selection, it is possible that we underestimate the level of contamination in the $\pm 500 \text{ km s}^{-1}$ window. In particular, the 25 cMpc box is too small to contain massive clusters, for which the galaxy peculiar velocities possibly reach $\sim 1000 \text{ km s}^{-1}$. In addition, the Mg II gas could still be “mis-assigned” even if it resides within r_{vir} of the assumed host, because the Mg II could arise in an undetected satellite galaxy. Therefore, the Mg II mis-assignment problem can be even worse in observational analyses.

From the observers’ perspective, whether the mis-assigned Mg II gas “detected” in a column (analogous to a sightline) significantly affects the Mg II measurements, e.g., column density and velocity dispersion, depends on the relative column density difference between the mis-assigned Mg II gas and the Mg II gas within r_{vir} . For example, if the column density of the Mg II gas inside of r_{vir} is orders-of-magnitude higher than that of the mis-assigned Mg II gas, then the mis-assigned Mg II gas will increase the overall velocity spread but have negligible effect on the total column density measured. Therefore, we repeat the calculation of the Mg II mis-assignment fraction by adding column density ratio requirements while flagging the “detected” mis-assigned Mg II gas; we require the column density of the mis-assigned Mg II gas to reach either at least 10% or 100% of that of the Mg II gas within r_{vir} . However, we find that adding either requirement only decreases the Mg II mis-assignment fractions by no more than 0.03 in magnitude compared to those in Figure 4. This suggests that a single column rarely intersects high density Mg II gas both within and outside of r_{vir} . The major observational consequence of the mis-assigned Mg II gas is the increase in the Mg II detection rate, i.e., the binary classification of detection vs. non-detection, rather than increasing the column density and/or velocity spread in individual columns (sightlines) that already detect Mg II gas from inside r_{vir} .

4. MORPHOLOGY AND ROTATION OF THE Mg II GAS

Although quasar sightline observations reveal the inhomogeneous distribution of the Mg II gas (Bouché et al. 2012; Kacprzak et al. 2012) and the corotation between the Mg II gas and galactic disks (Ho et al. 2017; Martin et al. 2019; Zabl et al. 2019), these observations do not uniquely identify the Mg II morphological structure nor the extent of the corotation. For example, is the Mg II gas isotropically distributed around the galaxy, or does the gas resemble a disk structure? In this section, we

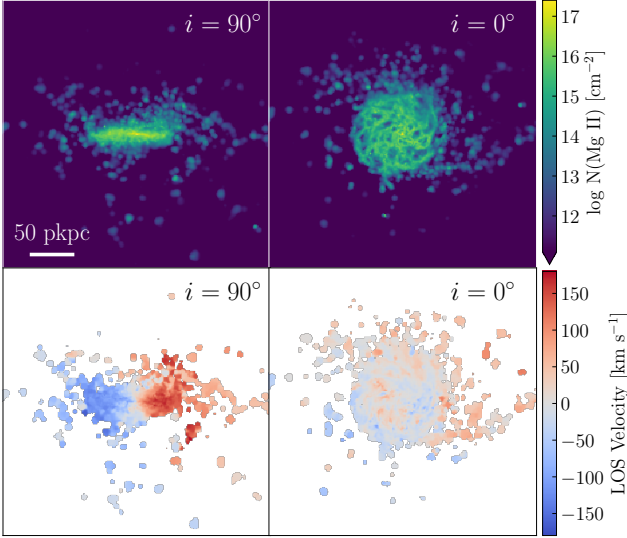


Figure 5. Mg II column density and LOS velocity maps of a star-forming galaxy of $\log(M_*/M_\odot) = 9.93$. This galaxy is projected at $i = 90^\circ$ (left) and 0° (right). The top and bottom rows show the Mg II column density and the Mg II-column-density-weighted LOS velocity, respectively. A positive (negative) LOS velocity indicates the gas is receding (approaching). These projection maps illustrate that the Mg II gas is morphologically and kinematically “disky”. Regions with Mg II gas below the detection limit of $N_{\text{MgII}} = 10^{11.5} \text{ cm}^{-2}$ are shown in purple and white on the column density and LOS velocity maps, respectively. Only the Mg II gas within r_{vir} of the galaxy is included. All maps have the same scale with 300 pkpc on each side.

examine the distribution of the corotating Mg II gas and study its morphological and rotation structures around galaxies. We analyze how these results vary with galaxy properties, and we also discuss how the mis-assigned Mg II gas affects our analysis.

We make 2D projection maps of the Mg II column density and the LOS velocity (weighted by the Mg II column density) to study the Mg II morphology and kinematics. We use the net specific angular momentum vector of the star particles \mathbf{j}_* to define how we project the galaxies (Section 2.2). For each galaxy, we orient \mathbf{j}_* such that it has components along the $+y$ (upward on the 2D map) and the $-z$ axes (into the 2D map) but not along the x -axis. This orientation makes the $+x$ -direction the receding side of the net rotation. We project each galaxy at fixed inclination angles of $i = 90^\circ, 60^\circ, 30^\circ$, and 0° , where i is the angle between \mathbf{j}_* and the $-z$ -axis of the 2D map. For example, for the $i = 0^\circ$ (90°) projection, \mathbf{j}_* points along the $-z$ -axis ($+y$ -axis).

Figure 5 illustrates the 2D projections of a star-forming galaxy with $M_* \approx 10^{10} M_\odot$. The Mg II column density maps (top row) at $i = 90^\circ$ and 0° show that the

Mg II distribution resembles that of an axis-symmetric disk viewed at edge-on and face-on, respectively. The bottom left panel shows the $i = 90^\circ$ projection of the Mg II LOS velocity. Not only do the blueshifted and redshifted sides indicate rotation, but the sense of rotation also follows that of the stellar component of the galaxy, i.e., the $x > 0$ side is redshifted and thereby receding. In particular, within the radius of around 50 pkpc, the rotation signature largely disappears at $i = 0^\circ$ (bottom right), an unsurprising outcome from the projection effect of disk rotation. A weak signature of rotation is still visible especially at large radii, however, suggesting that how well the Mg II gas corotates with the stellar component of the galaxy depends on radius. Nevertheless, from both morphological and kinematic perspectives, this example galaxy has a disk-like Mg II structure.

4.1. Morphological Structure of Mg II Gas

We examine how the morphology and radial extent of the Mg II gas vary with galaxy stellar masses and differ between star-forming and quiescent galaxies. We project each galaxy at fixed inclination angles, and we produce the corresponding column density maps of the Mg II gas within r_{vir} . Then, we stack these individual maps based on whether the galaxies are star-forming or quiescent and their stellar masses. For each pixel of each stack, we count the number of galaxies with Mg II gas “detected”, i.e., $\log N_{\text{MgII}}[\text{cm}^{-2}] \geq 11.5$, and divide it by the total number of galaxies within the stack. This generates a map of the “Mg II detection fraction”, which varies between 0 and 1 if none or all of the galaxies within the stack have “detected” Mg II gas. The maps in Figures 6 and 7 show the median Mg II column density and the Mg II detection fraction, respectively, of all star-forming galaxies from $10^9 M_\odot$ to $10^{11} M_\odot$ (columns) and at inclination angles of $i = 90^\circ, 60^\circ, 30^\circ$, and 0° (rows).

Figures 6 and 7 demonstrate two properties of the Mg II distribution around star-forming galaxies. First, the Mg II gas is not spherically distributed. The Mg II morphology changes with the projection angle of the galaxies; for galaxies projected at higher (lower) inclination angles, the column density maps show that the Mg II distribution is more flattened (isotropic), and the contours of the Mg II detection fraction are more elliptical (circular). This is contrary to the circular contours expected on both sets of the 2D maps at all projection angles if the Mg II gas were spherically distributed. The median column density maps in Figure 6 largely resemble that of the galaxy example in Figure 5 and show that the Mg II gas is morphologically “disky” on average. These average maps illustrate that the detectable Mg II gas possibly extends further away from the mid-

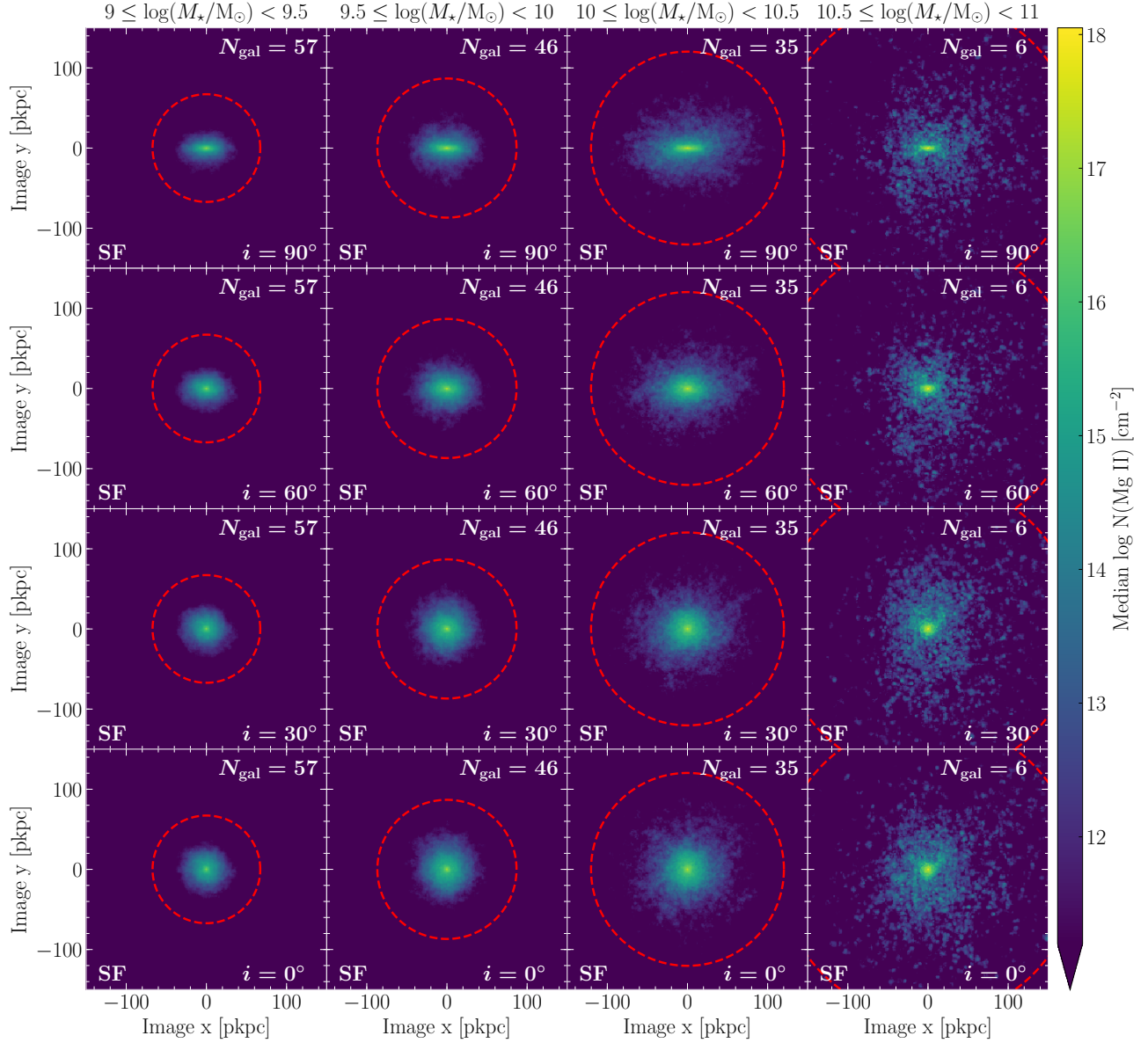


Figure 6. Median Mg II column density around star-forming galaxies projected at different inclination angles and grouped into different stellar mass bins. Only the gas within r_{vir} of individual galaxies is included. From left to right, each column shows the result for galaxies with increasing stellar masses (labeled at the top of each column). Each row represents galaxies projected at different inclination angles i before stacking (labeled at the lower right of each panel). The number of galaxies N_{gal} in each stack is labeled at the upper right. Each red dashed circle shows the median $0.5r_{\text{vir}}$ of the galaxies in the stack. The Mg II gas is clearly not spherically distributed.

plane than that of the example galaxy, e.g., see the $10 \leq \log(M_*/M_\odot) < 10.5$ panels. In fact, the Mg II detection fraction maps demonstrate that even at the $i = 90^\circ$ projection (top row of Figure 7), over 50% of the galaxies (green contours) have detectable Mg II gas at least 20 pkpc above the midplane, which is an order-of-magnitude thicker than gas disks with a typical scaleheight of $\lesssim 2$ kpc (van der Kruit & Freeman 2011; Kamphuis et al. 2013; Zschaechner et al. 2015). Therefore, the shape of the contours of both the column

density and detection fraction maps implies that generally neither a sphere nor a thin disk describes the Mg II gas (further discussed in Section 5).

Secondly, the Mg II gas is more extended around star-forming galaxies with higher masses than around those with lower masses. The detection fraction maps clearly demonstrate this trend. For example, 50% of the $10 \leq \log(M_*/M_\odot) < 10.5$ galaxies (green contours) “detect” Mg II gas out to about 85 pkpc, but none of the $9 \leq \log(M_*/M_\odot) < 9.5$ galaxies “detect” Mg II gas at the

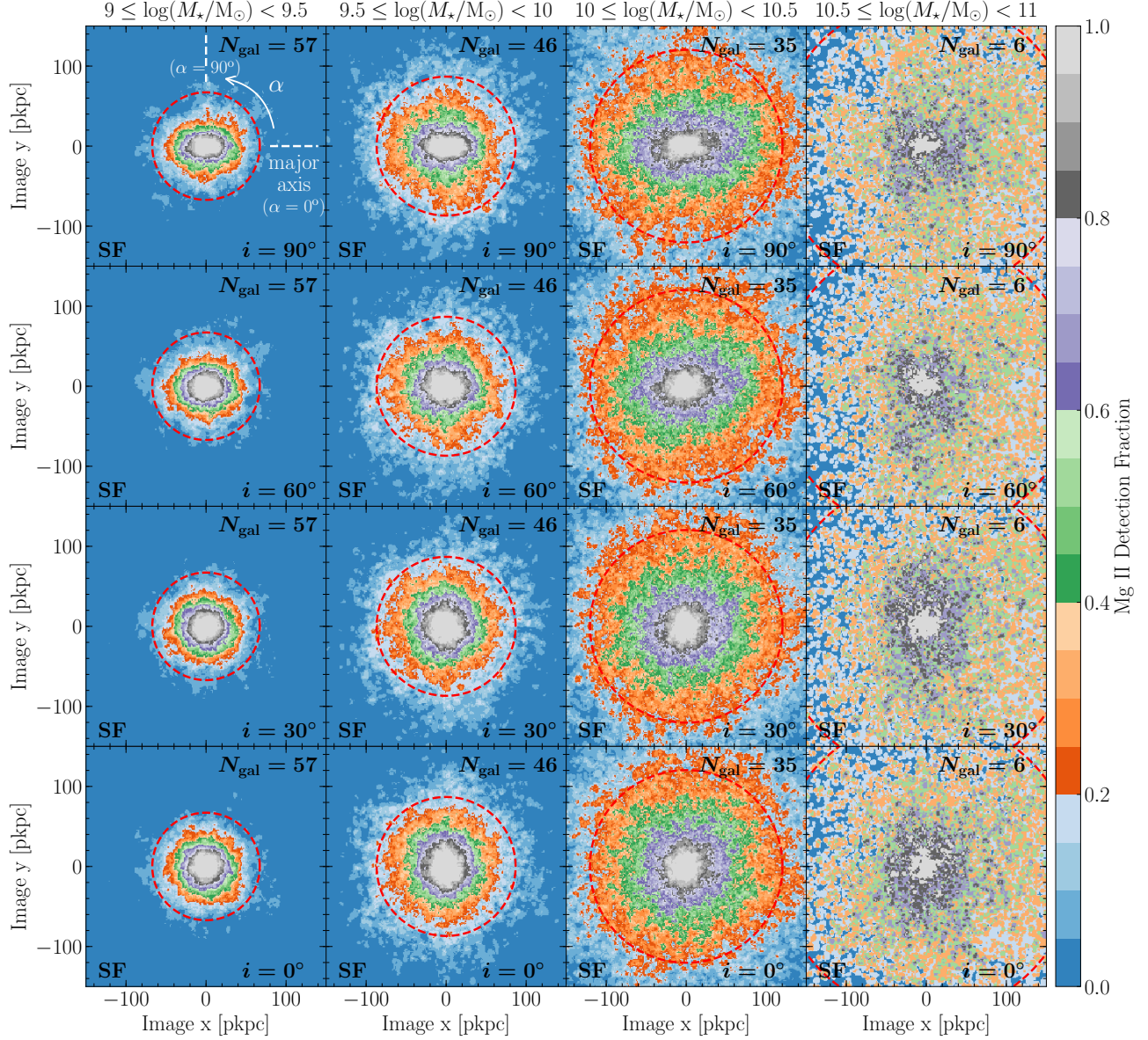


Figure 7. Mg II detection fraction of star-forming galaxies projected at different inclination angles and grouped into different stellar mass bins. The color maps represent the Mg II detection fraction, which is calculated by dividing for each pixel the number of galaxies with Mg II gas “detected” ($N_{\text{MgII}} \geq 10^{11.5} \text{ cm}^{-2}$) by the total number of galaxies within the stack (labeled at the upper right of each panel). Similar to Figure 6, each column shows the result for galaxies with different stellar masses, and each row represents galaxies projected at different inclination angles i before stacking. Each red dashed circle shows the median $0.5r_{\text{vir}}$ of the galaxies in the stack. The Mg II gas is not spherically distributed and extends to larger radii for more massive galaxies. This analysis only includes the Mg II gas within r_{vir} of individual galaxies.

same radius. The trend becomes less clear for the $10.5 \leq \log(M_*/M_\odot) < 11$ galaxies; this is possibly due to small number statistics with only six galaxies in the stack, which also explain the less symmetric detection fraction contours compared to other mass bins. Nonetheless, recall that we have only included the gas within r_{vir} . The trend is observed not only in terms of the physical size (i.e., pkpc) but also relative to the size of the virial halo. The red dashed circle in each panel shows the median

$0.5r_{\text{vir}}$ of the galaxies in the stack. The Mg II gas around higher mass galaxies still extends to larger radii relative to r_{vir} compared to lower mass galaxies (also see Figure A.1 in the Appendix).

We repeat the same analysis for quiescent galaxies. Figures 8 and 9 show the 2D maps of the median Mg II column density and the Mg II detection fraction, respectively, for quiescent galaxies projected at $i = 90^\circ$. We caution that each stellar mass bin only has a few quies-

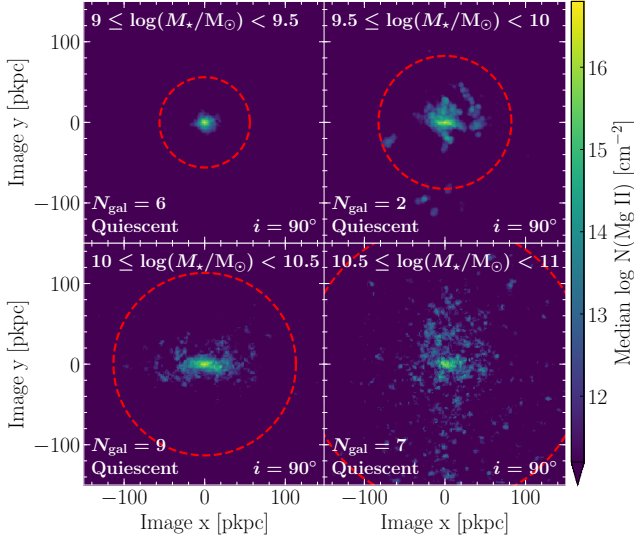


Figure 8. Median Mg II column density around quiescent galaxies at $i = 90^\circ$ projection. This plot is similar to the first row of Figure 6, but different panels show the stack of quiescent galaxies with different stellar masses. The number of galaxies N_{gal} in each stack is labeled at the lower left. Each red dashed circle shows the median $0.5r_{\text{vir}}$ of the galaxies in the stack. This analysis only includes the Mg II gas within r_{vir} of individual galaxies.

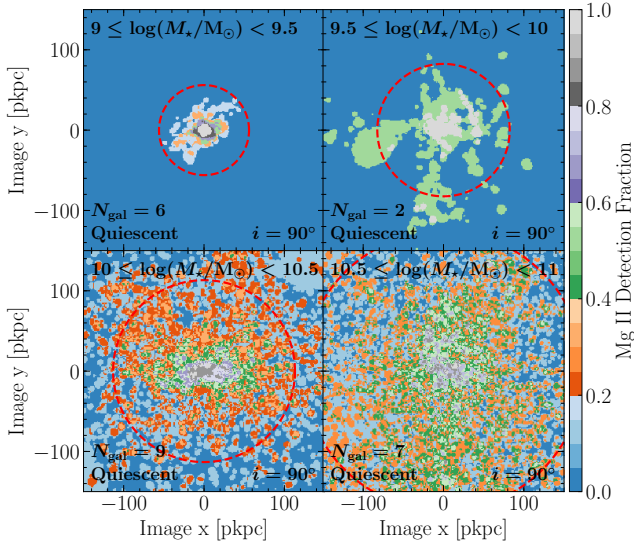


Figure 9. Mg II detection fraction around quiescent galaxies at $i = 90^\circ$ projection. This plot is similar to the first row of Figure 7, but different panels show the stack of quiescent galaxies with different stellar masses. The number of galaxies N_{gal} in each stack is labeled at the lower left. Each red dashed circle shows the median $0.5r_{\text{vir}}$ of the galaxies in the stack. This analysis only includes the Mg II gas within r_{vir} of individual galaxies.

cent galaxies (Table 2), so the results may be subject to

small number statistics. Nevertheless, around quiescent galaxies with higher masses, the Mg II gas has larger radial extent in both physical size and relative to r_{vir} (also see Figure A.2 in the Appendix). While Figures 8 and 9 seem to suggest that the Mg II distribution around quiescent galaxies is patchy, the patchiness of the Mg II gas around individual galaxies will be washed out for a large number of galaxies, creating a smooth distribution on average. In fact, for each mass bin, if we randomly select the same number of star-forming galaxies as quiescent galaxies, then the maps for star-forming galaxies also show patchier and less regular Mg II gas distributions than Figures 6 and 7. We also note that there exist $10 \leq \log(M_*/M_\odot) < 10.5$ quiescent galaxies with Mg II gas preferentially residing near the midplane; this pattern is also illustrated in the median column density map (lower left panel of Figure 8). But overall, the Mg II gas around quiescent galaxies is potentially more isotropically distributed compared to that around star-forming galaxies.

While the Mg II detection fraction analysis has been focusing on the gas within r_{vir} of individual galaxies, observational studies typically associate Mg II gas with galaxy hosts using a fixed LOS velocity window $|\Delta v_{\text{LOS}}|$. Because this potentially selects mis-assigned Mg II gas outside of r_{vir} (see Section 3), we explore how the mis-assigned Mg II gas affects our results. Following Section 3, we select the Mg II gas within $|\Delta v_{\text{LOS}}| = 500 \text{ km s}^{-1}$ from the galaxy systemic velocity and repeat the detection fraction calculations. As an illustration, Figure B.1 in the Appendix shows the new Mg II detection fraction maps for $i = 90^\circ$ star-forming galaxies. Comparing them with the original maps obtained from the Mg II gas within r_{vir} (first row of Figure 7), the new light blue patches near the edge of the maps ($\gtrsim 0.5r_{\text{vir}}$) indicate that the detection fraction at these regions increases from around 0 to $\lesssim 0.1$.

Figure 10 shows the Mg II detection fractions for $i = 90^\circ$ (top) and 0° (bottom) star-forming galaxies as a function of impact parameter. The solid and dashed curves represent the Mg II detection fraction calculated from the gas within r_{vir} and within the $|\Delta v_{\text{LOS}}| = 500 \text{ km s}^{-1}$ window of individual galaxies, respectively. We also bin the results by azimuthal angle α , which is the angle between the galaxy major axis (x -axis on the map) and the line joining the center of the galaxy and each pixel; see the illustration in the top left panel of Figure 7. The darker (lighter) line represents smaller (larger) azimuthal angles, i.e., closer to the galaxy major (minor) axes. First, regardless of how the gas is selected, the Mg II detection fraction at a fixed impact parameter is higher (lower) at smaller (larger)

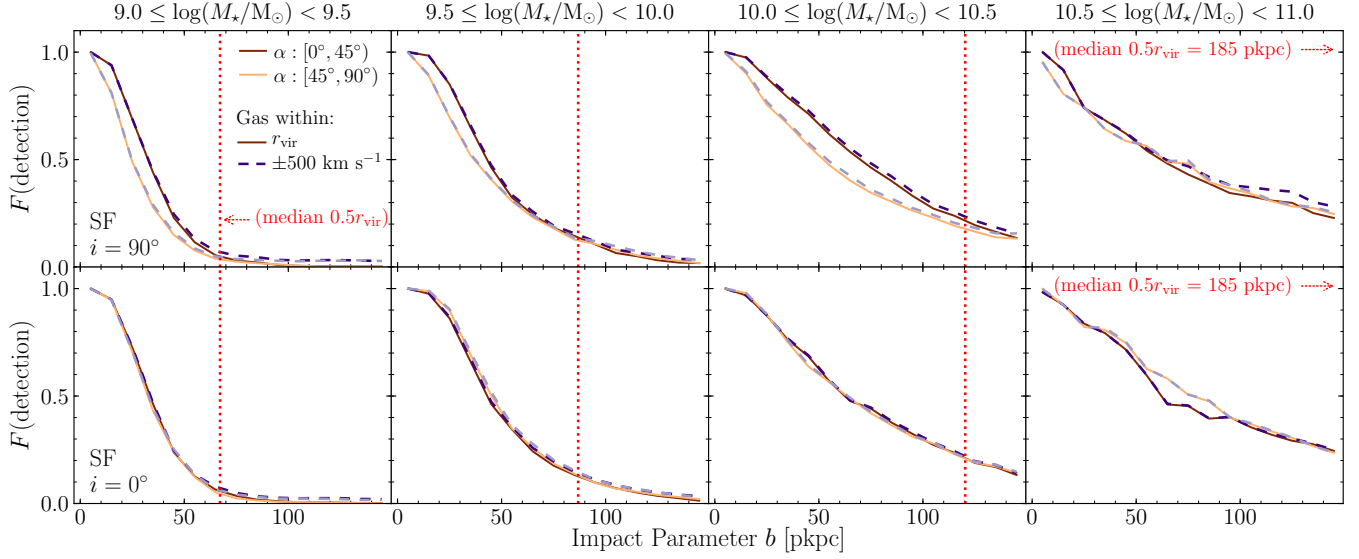


Figure 10. Mg II detection fraction as a function of impact parameter b for star-forming galaxies projected at $i = 90^\circ$ (i.e., seen edge-on, top row) and 0° (i.e., seen face-on, bottom row). In each panel, the solid and dashed curves represent the detection fractions obtained from gas physically within r_{vir} and within $|\Delta v_{\text{LOS}}| = 500 \text{ km s}^{-1}$ from the galaxy systemic velocity, respectively. The darker (lighter) curve represents the azimuthal angle α range of $0^\circ \leq \alpha < 45^\circ$ ($45^\circ \leq \alpha < 90^\circ$), i.e., closer to the galaxy major (minor) axes. The vertical red dotted line shows the median $0.5r_{\text{vir}}$ of the galaxies in the stack.

azimuthal angle when the galaxies are projected edge-on (i.e., $i = 90^\circ$). Such difference largely disappears in face-on ($i = 0^\circ$) galaxy projections. This reiterates the result that Mg II gas is not spherically distributed but preferentially resides near the midplane. Second, for the same azimuthal angle bin, selecting Mg II gas at $|\Delta v_{\text{LOS}}| \leq 500 \text{ km s}^{-1}$ (dashed) produces a higher Mg II detection fraction than selecting Mg II gas physically within r_{vir} (solid). The difference is around 0.02 in magnitude and is more obvious at large impact parameters (e.g., $\gtrsim 0.5r_{\text{vir}}$); the 0.02 difference represents an increase of over tens of percent at impact parameters where the Mg II within r_{vir} produces a low detection fraction. Hence, our result implies that the mis-assigned Mg II gas will elevate the Mg II detection rate measured in random sightlines around galaxies. As we will show in Section 4.2, the mis-assigned gas has a more significant effect on detecting corotating Mg II gas.

4.2. Rotational Structure of the Mg II Gas

Motivated by observational studies showing corotation between the Mg II gas and the galaxy disk, we focus on the Mg II gas that corotates with the EAGLE galaxies and examine the corotating gas structure. Similar to calculating the Mg II detection fraction, here we determine the fraction of Mg II that is corotating and detectable. We project each galaxy at fixed inclination angles and produce the Mg II-column-density-weighted LOS velocity maps. Because we orient the galaxies with

the receding side at the $+x$ -direction, a $x > 0$ (< 0) pixel with a net redshift (blueshift) indicates corotation. We flag the pixels with Mg II gas “detected” ($\log N_{\text{MgII}}[\text{cm}^{-2}] \geq 11.5$) and corotating. Then, at every pixel of each galaxy stack, we count the number of galaxies flagged and divide it by total number of galaxies in the stack. The outcome measures how often we “detect” corotating Mg II gas among all galaxies.

Figure 11 shows the fraction of Mg II gas within r_{vir} of star-forming galaxies that is corotating and detectable. Different rows and columns show the results for different galaxy inclination angles and stellar mass bins, respectively. We do not show the $i = 0^\circ$ projection, because the fraction of Mg II that is corotating and detectable becomes an ill-defined quantity at $i = 0^\circ$; the question of whether the detectable Mg II gas at individual $x > 0$ (< 0) pixel shows a net redshift (blueshift) matches with that expected from an $i = 0^\circ$ rotating disk is ill-defined, because the latter produces zero Doppler shift, i.e., neither blueshifted nor redshifted. Comparing different columns of Figure 11 shows that for more massive galaxies, Mg II gas is more frequently detectable and corotating at large projected radii compared to less massive galaxies. The trend becomes less clear for the highest mass bin of $10.5 \leq \log(M_*/M_\odot) < 11$, mostly likely due to small number statistics with only a few galaxies in the stack. Nevertheless, in general, both the Mg II detection fraction and the fraction of Mg II that is corotating and detectable demonstrate the same trend that

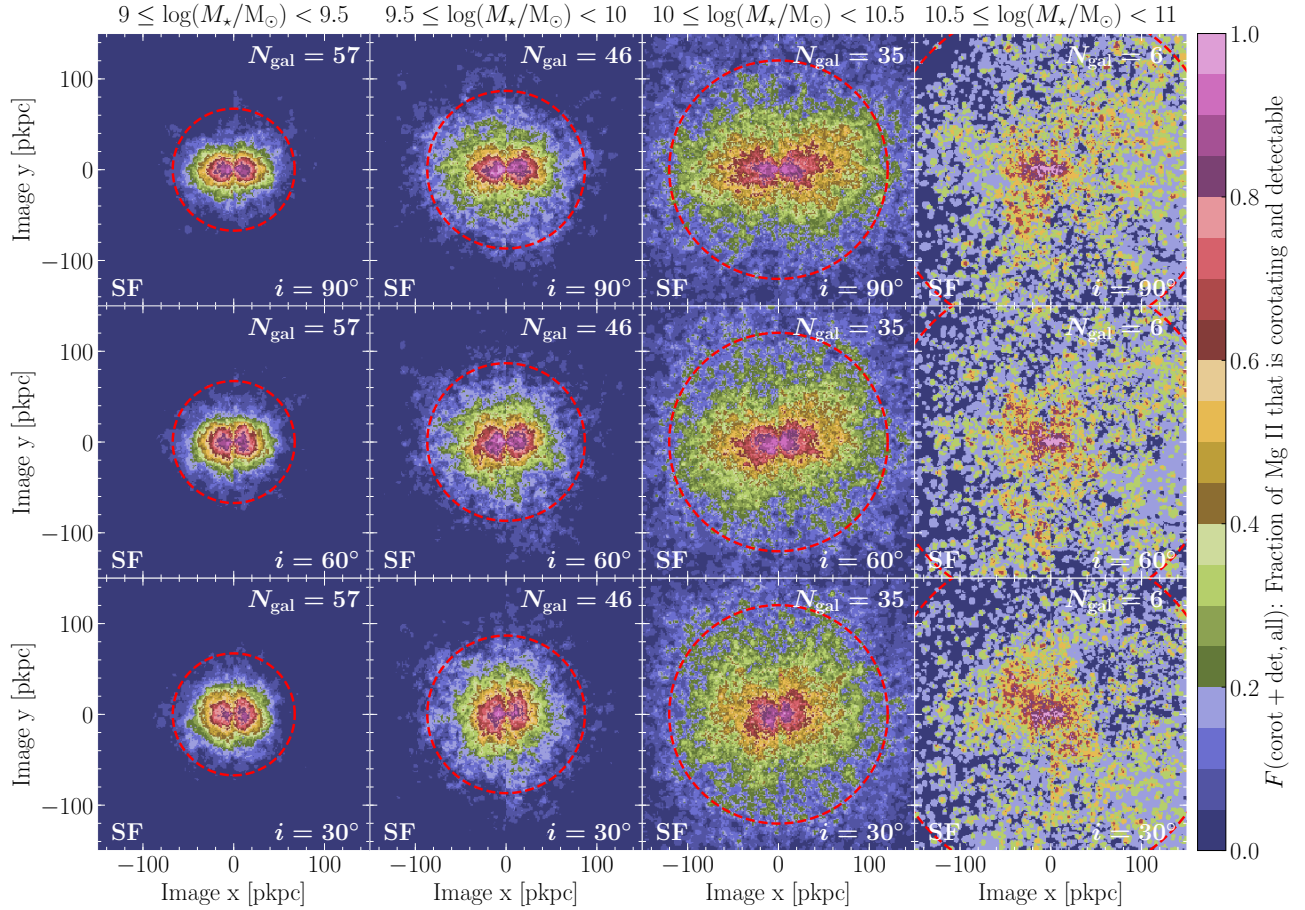


Figure 11. Fraction of Mg II that is corotating and detectable for star-forming galaxies projected at different inclination angles and grouped into different stellar mass bins. The color maps represent the fraction of Mg II that is corotating and detectable, which is calculated by dividing the number of galaxies with Mg II gas “detected” ($N_{\text{MgII}} \geq 10^{11.5} \text{ cm}^{-2}$) and corotating by the total number of galaxies in the stack (labeled at the upper right of each panel). Each column shows the result for galaxies in a different stellar mass bin (labeled at the top of each column). Each row represents galaxies projected at a different inclination angle i before stacking (labeled at the lower right of each panel). Each red dashed circle shows the median $0.5r_{\text{vir}}$ of the galaxies in the stack. This analysis only includes the Mg II gas within r_{vir} of individual galaxies.

(corotating) Mg II gas is more extended around higher mass galaxies (at least for galaxies with $\log(M_*/M_\odot) < 10.5$).

While the contour shape of the Mg II corotation maps in Figure 11 also changes with the projected inclination angles, the contours take a different shape from those of the detection fraction. Especially near the galaxy center and regions with high fractions of corotating and detectable Mg II (e.g., $\geq 50\%$), the contours resemble a dumbbell shape with the two lobes lying along the galaxy major axis (i.e., x -axis on the map). This implies that the fraction of Mg II that is corotating and detectable is reduced near the galaxy minor axis; we will discuss possible explanations (e.g., outflows) in Section 5.2.

Instead of showing the 2D maps, the top row of Figure 12 shows the fraction of Mg II that is corotating and

detectable as a function of impact parameter for star-forming galaxies at the $i = 90^\circ$ projection. Similar to Figure 10, the darker (lighter) curve represents smaller (larger) azimuthal angle α , i.e., closer to the galaxy major (minor) axes. The solid and dashed curves show the results obtained from the Mg II gas within r_{vir} and within $|\Delta v_{\text{LOS}}| = 500 \text{ km s}^{-1}$ from the systemic velocity of individual galaxies, respectively. Regardless of which Mg II selection method we use, clearly for all mass bins (shown in separate panels), the fraction decreases towards the galaxy minor axis for a fixed impact parameter. This indicates a paucity of net corotating Mg II gas towards the minor axis.

While the fraction of Mg II that is corotating and detectable decreases sharply with impact parameter and does not seem to depend on how we select the Mg II gas, we emphasize that this steep decline largely results

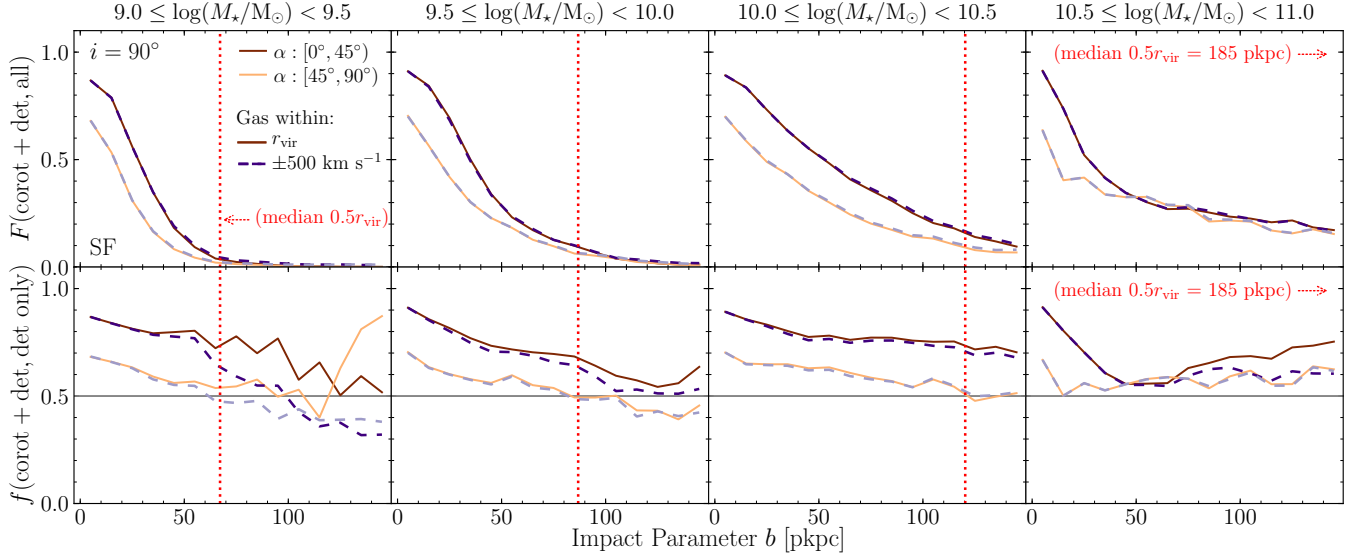


Figure 12. Fractions of corotating Mg II as a function of impact parameter b for star-forming galaxies projected at $i = 90^\circ$ (i.e., seen edge-on). The top row shows the fraction of Mg II that is corotating and detectable calculated using all pixels in individual galaxy stacks, $F(\text{corot} + \text{det}, \text{all})$. The bottom row shows the fraction of detectable Mg II that is corotating, $f(\text{corot} + \text{det}, \text{det only})$, which is calculated using only the pixels with detectable Mg II. Different columns show the results for different stellar mass bins. In each panel, the darker (lighter) line represents the azimuthal angle α range of $0^\circ \leq \alpha < 45^\circ$ ($45^\circ \leq \alpha < 90^\circ$), i.e., closer to the galaxy major (minor) axes. The solid and dashed curves represent the fractions obtained from gas physically within r_{vir} and within $|\Delta v_{\text{LOS}}| = 500 \text{ km s}^{-1}$ from the galaxy systemic velocity, respectively. The vertical red dotted line shows the median $0.5r_{\text{vir}}$ of the galaxies in the stack. At a fixed impact parameter, both the top and bottom rows show that the fraction of corotating Mg II gas increases towards the galaxy major axis. The difference between selecting Mg II gas within $|\Delta v_{\text{LOS}}|$ and r_{vir} becomes prominent at impact parameters $\gtrsim 0.25r_{\text{vir}}$.

from the sharp drop in the detection fraction. In other words, it does not necessarily imply a transition of the Mg II gas from having a net corotation to a lack thereof. Our calculation is analogous to examining how often we “detect” corotating Mg II gas for random sightlines around galaxies. But from the observers’ perspective, the more interesting question is how often they measure a net corotation in sightlines that detected Mg II gas (e.g., [Martin et al. 2019](#), also see the Ly α “corotation fraction” analysis in [French & Wakker 2020](#)). Therefore, we modify our calculation to answer this question. Instead of dividing the number of galaxies with corotating Mg II “detected” by the total number of galaxies in the stack, we divide it by the number of galaxies with “detected” Mg II gas. The outcome represents the fraction of detectable Mg II gas that is corotating.

The bottom row of Figure 12 shows the fraction of detectable Mg II gas that is corotating as a function of impact parameter for $i = 90^\circ$ star-forming galaxies. Clearly, the results depend on whether we select the gas that is within r_{vir} (solid) or within the $|\Delta v_{\text{LOS}}| = 500 \text{ km s}^{-1}$ window (dashed). While the results from both Mg II selections share some characteristics, such as exhibiting an azimuthal dependence and declining slightly with impact parameter, the difference between

using the two selection methods becomes prominent at impact parameters beyond $\approx 50 \text{ pkpc}$ or $0.25r_{\text{vir}}$. Compared to selecting the Mg II gas within r_{vir} , the Mg II gas selected by $|\Delta v_{\text{LOS}}| \leq 500 \text{ km s}^{-1}$ has a lower fraction of detectable Mg II gas that is corotating. This means that the Mg II outside of r_{vir} reduces the frequency of detecting net corotating Mg II gas at a fixed impact parameter. We will discuss how this impacts the observational analysis of corotating Mg II gas in Section 5.1. We caution that especially in the lowest mass bin, although the fraction obtained from gas within r_{vir} (solid) shows a slight increase at large impact parameters ($\gtrsim 130 \text{ pkpc}$), this is due to the rare Mg II detection (Figure 10), which makes the measured fraction of detectable Mg II that is corotating very noisy.

As for the quiescent galaxies, it is less clear whether or not their Mg II gas is generally rotating as is the case for the star-forming galaxy counterparts. Figure 13 shows the fraction of Mg II that is corotating and detectable for quiescent galaxies projected at $i = 90^\circ$ (analogous to the top row of Figure 11), and the contours do not show a particular pattern. This could again be a result of small number statistics, which we have already seen in the detection fraction maps. But still, there exist quiescent galaxies of $10 \leq \log(M_*/M_\odot) < 10.5$ having Mg II

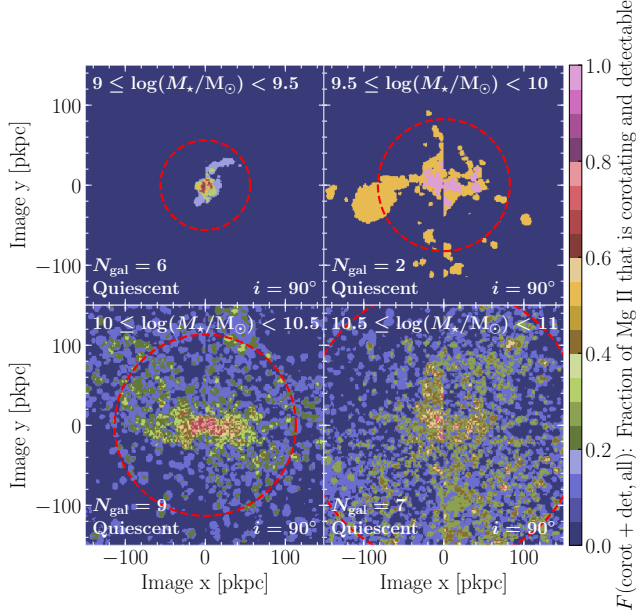


Figure 13. Fraction of Mg II that is corotating and detectable for quiescent galaxies at $i = 90^\circ$ projection. Each panel shows the galaxy stack of different mass bins. The number of galaxies N_{gal} in each stack is labeled at the lower left. Each red dashed circle shows the median $0.5r_{\text{vir}}$ of the galaxies in the stack. This analysis only includes the Mg II gas within r_{vir} of individual galaxies.

gas that is morphologically and kinematically “disky”. This can be seen marginally in Figure 13, but the contours are too irregular to make a general description. Hence, the Mg II detection fraction and the fraction of Mg II that is corotating and detectable potentially suggest that quiescent and star-forming galaxies have different Mg II morphology and kinematic structure, but the poor statistics for quiescent galaxies make this result inconclusive.

5. DISCUSSION

We have shown that how the detection fraction of Mg II and the identification of corotating Mg II gas vary with galaxy properties. We have also raised the concern that the Mg II gas selected by a LOS velocity window ($|\Delta v_{\text{LOS}}| \leq 500 \text{ km s}^{-1}$) but physically outside of r_{vir} , i.e., the mis-assigned Mg II gas, possibly affects the observational analysis of the CGM. In this section, we will discuss how this mis-assigned Mg II gas affects the observational analysis of corotating gas in sightline studies. We will also interpret our results regarding the morphological and kinematic structure of the Mg II gas and discuss recent related work in observations and simulations.

5.1. How does the mis-assigned Mg II gas affect the Mg II detection and corotation analysis in observational studies?

Quasar sightline studies have established the steep decline in the covering factor (i.e., detection rate) and the strength of the Mg II absorption systems with impact parameter (Chen et al. 2010; Nielsen et al. 2013a; Lan et al. 2014; Lan & Mo 2018; Huang et al. 2020). Our Mg II detection fraction analysis agrees with this result. However, we also demonstrated that if we select the Mg II gas using the $|\Delta v_{\text{LOS}}| = 500 \text{ km s}^{-1}$ window instead of requiring the gas to be physically within r_{vir} , then the detection fraction increases by around 0.02 in magnitude. This can correspond to an increase of several tens of percent for lower mass galaxies and at large impact parameters (e.g., $\gtrsim 100 \text{ pkpc}$), where the gas within r_{vir} only gives a low Mg II detection fraction of the order of 0.01 (Figure 10). As a result, the increase in detection fraction at large radii makes the circumgalactic Mg II gas seem more extended around galaxies than it is. Because observers often use $|\Delta v_{\text{LOS}}|$ to identify the Mg II gas around target galaxies, the mis-assigned Mg II gas outside of r_{vir} will increase the number of Mg II systems detected and/or the strength of Mg II systems measured at large radii. This potentially affects the anticorrelation between covering fraction (and Mg II strength) and impact parameter derived from quasar sightline observations, such as increasing the uncertainties of the fit between the two quantities or weakening the anticorrelation.

The mis-assigned Mg II gas outside of r_{vir} but within the $|\Delta v_{\text{LOS}}|$ window has a significant effect on identifying corotating Mg II gas. The bottom row of Figure 12 shows the fraction of detectable Mg II gas that is corotating as a function of impact parameter. From the observers’ perspective, this fraction represents how likely it is to find corotating Mg II gas in Mg II detected sightlines. If sightlines intersect randomly moving gas, then there should be an equal number of sightlines intersecting corotating and non-corotating gas. Hence, at a fixed impact parameter, observers expect to detect the fraction exceeding 0.5 if the Mg II gas generally has a net corotation (grey horizontal lines). At impact parameters beyond $\approx 50 \text{ pkpc}$ or $0.25r_{\text{vir}}$, the plots show that the fraction is lower when the Mg II gas is selected by $|\Delta v_{\text{LOS}}|$ (dashed) instead of within r_{vir} (solid). For example, near the major axis ($\alpha < 45^\circ$) of the $9.0 \leq \log(M_*/M_\odot) < 9.5$ star-forming galaxies, the fraction drops to 0.5 at 100 pkpc if we select the Mg II gas by $|\Delta v_{\text{LOS}}|$, but the detectable Mg II within r_{vir} actually shows net corotation out to 130 pkpc ($\approx r_{\text{vir}}$). Observers typically identify the Mg II gas around target

galaxies using the $|\Delta v_{\text{LOS}}|$ window. Therefore, our result implies that at large impact parameters where Mg II gas is less often detected, observers will measure a lower detection rate of Mg II corotating gas among the Mg II detected sightlines, because the mis-assigned Mg II gas contaminates the signal. This leads observers to underestimate the spatial extent of Mg II corotating gas, i.e., the measured fraction of detectable Mg II that is corotating drops below 0.5 at too small of an impact parameter.

5.2. Coherent Mg II Gas Structure Around Star-forming Galaxies

While we have illustrated that Mg II gas disks exist (e.g., Figure 5), the median Mg II column density maps (Figure 6) and detection fraction maps (Figure 7) indicate that a thin disk does not describe the typical Mg II distribution around star-forming galaxies. The Mg II gas clearly does not have a spherical distribution either, because the contours are non-circular with their shape changing with the galaxy inclination projection angle. Instead, the maps show that the Mg II gas distribution is axisymmetric. Furthermore, in regions near the projected galaxy major axes (galaxy orientation defined by \hat{j}_\star), the corotating Mg II gas is more frequently detected. The contours of the Mg II corotation maps show two lobes aligning with the galaxy major axes (Figure 11), and the 1D profiles also show that at a fixed impact parameter, the fraction of detectable Mg II that is corotating decreases with increasing azimuthal angle (bottom row of Figure 12). Altogether, these results not only show that the Mg II gas is not spherically distributed and has an axisymmetric structure, but that the axis of symmetry aligns with that of the rotation of the stars and the Mg II gas. In fact, the 50% contours of the Mg II detection fraction suggest that for half of the galaxies, these rotating Mg II structures possibly reach over 20 pkpc from the midplane. An axisymmetric, rotating Mg II structure can also explain the low fraction of corotating and detectable Mg II gas at large azimuthal angles, i.e., near the projected galaxy minor axes. Because the projected velocity from the tangential velocity component is small near the minor axis, any turbulence overwhelms the net corotation signature and decreases the rate of detecting the corotating gas.

A possible source of turbulence is a wind blown out perpendicular to the disk plane (De Young & Heckman 1994) that kinematically disturbs the CGM (Heckman et al. 2017; Martin et al. 2019). Around the EAGLE galaxies, we find the signature of hot winds from the higher gas temperature in the biconical regions above and below the disk plane. As an illustration, the left

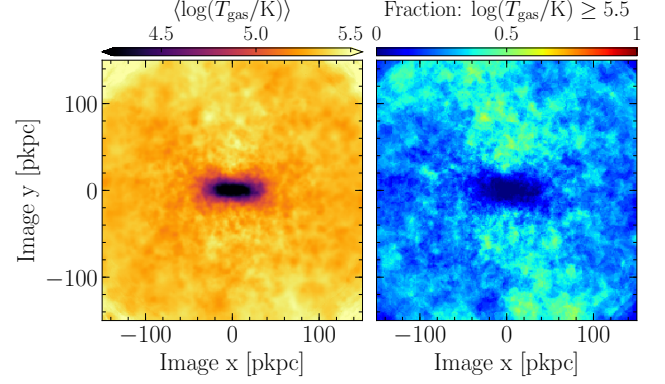


Figure 14. Average temperature of gas within r_{vir} of the $9.5 \leq \log(M_\star/M_\odot) < 10.0$ star-forming galaxies projected at $i = 90^\circ$. (left) Mean gas temperature $\langle \log(T_{\text{gas}}/\text{K}) \rangle$ of the stacked galaxies. (right) Fraction of galaxies with $\log(T_{\text{gas}}/\text{K}) \geq 5.5$. Both panels illustrate that gas near the projected galaxy minor axes typically has a higher temperature.

panel of Figure 14 shows the higher mean gas temperature ($\langle \log T_{\text{gas}} \rangle$) near the minor axes of the $9.5 \leq \log(M_\star/M_\odot) < 10.0$ star-forming galaxies. Similarly, the right panel shows a higher fraction of galaxies with average gas temperature $\geq 10^{5.5}$ K (cyan) near the minor axes. The higher temperature near the minor axis also implies that the wind signature can be observed in the warm-hot and/or hot phases traced by higher ions, but this is beyond the scope of this paper. Mitchell et al. (2020) have also recently shown that the CGM of EAGLE galaxies typically exhibits a bipolar outflow pattern aligning with the galaxy minor axis (see their Figure 7).

It is worth noting that theoretical work and recent simulations have raised the concern of how the cool gas (e.g., traced by Mg II) survived entrainment by the hot winds (Schneider et al. 2018; Gronke & Oh 2020). Tackling this question requires simulations with parsec-scale resolution in the low-density CGM and has presented challenges for large-scale cosmological simulations. For example, both the high-resolution 25 Mpc EAGLE volume and TNG50 (Nelson et al. 2020, Figure 1) have an average comoving particle separation or gas resolution of about 1 kpc at densities of $n_{\text{H}} \sim 10^{-2} \text{ cm}^{-3}$, and the resolution worsens (improves) at lower (higher) density regions. Because most cosmological simulations focus the computational resources at denser regions and coarsely resolve the CGM, recent efforts applied new refinement schemes to enhance the CGM resolution in cosmological zoom simulations of individual objects. For example, van de Voort et al. (2019) used the AREPO moving-mesh hydrodynamics code (Springel 2010) with an additional uniform spatial refinement to force a minimum cell size

of 1 pkpc in their Milky Way mass galaxy simulations, whereas [Hummels et al. \(2019\)](#) and the FOGGIE simulations ([Peeples et al. 2019](#)) used the adaptive mesh refinement code ENZO ([Bryan et al. 2014](#)) with their independently developed refinement techniques and resolved spatial scales of about 500 comoving-pc out to 100 comoving-kpc in galactocentric radius. However, for the higher gas densities typical of low-ionization absorbers, the gains in resolution are modest relative to the simulation analyzed here. Future work achieving even higher resolution in dense gas will be important to shed further light on the survival of Mg II clouds.

Our picture of the axisymmetric, rotating Mg II circumgalactic gas around star-forming galaxies broadly agrees with recent results of CGM analyses using different cosmological simulations, all of which establish a picture of the rotating CGM with significant angular momentum. Using zoom-in simulations with the EAGLE model, [Huscher et al. \(2020\)](#) recently found that the angular momentum vectors between the hot and cold components of the CGM are well-aligned and better than that of the stellar disk at $z = 0$. They showed that the cold gas has a higher specific angular momentum than the hot gas. The tangential velocities of the cold gas (and metal) suggested that the cold gas is primarily rotationally supported out to 40 kpc in radius. The hot gas has a lower tangential velocity but still shows net rotation out to the radius of 50 kpc, implying that the hot CGM is poorly described by hydrostatic equilibrium ([Oppenheimer 2018](#)). The recent work of [DeFelippis et al. \(2020\)](#) also showed that the cold CGM has a higher specific angular momentum for $z \lesssim 2$ galaxies in IllustrisTNG. For their high- j_* (low- j_*) galaxy subsample, the angular momentum vector alignment between the stellar component and the CGM is stronger than (comparable to) that found in [Huscher et al. \(2020\)](#). In addition, they showed that winds and fountain gas dominated the biconical polar region, whereas the cold, high angular momentum gas occupied a wedge near the planar region on their single-quadrant 2D map. This led to their conclusion of a cylindrically symmetric CGM distribution. We note that their wedge is analogous to our two lobes along the galaxy major axis shown on the Mg II corotation maps (Figure 11). Earlier work by [Kauffmann et al. \(2016, 2019\)](#) also found a rotating CGM around Milky Way-like galaxies in both Illustris and IllustrisTNG. The CGM in Illustris rotates coherently over 70 kpc and has a larger vertical coherent length than that in IllustrisTNG, and the authors attributed the difference to the change in the feedback prescriptions.

The rotating CGM in cosmological simulations and our description of the axisymmetric, rotating Mg II gas structure support the interpretation and kinematic modeling from circumgalactic absorption measurements and share similarities with H I observations of nearby galaxies. Quasar sightline observations found Mg II gas corotating with the galaxy disk, but the Mg II gas spans broader velocity range than a thin rotating disk can explain ([Steidel et al. 2002](#); [Kacprzak et al. 2010, 2011](#); [Martin et al. 2019](#), etc.). Modeling the Mg II gas as a thick disk (with or without a rotation lag) with a height of over 20 kpc ([Steidel et al. 2002](#); [Kacprzak et al. 2010, 2011](#)) or combining it with a radial inflow component can plausibly reproduce the measured Mg II kinematics ([Ho et al. 2017](#); [Ho & Martin 2020](#)). On the one hand, these models defy the general perception of a disk. Stellar disks and gas disks typically have scale-heights below hundreds of parsec ([de Grijs 1998](#)) and $\lesssim 2$ kpc (e.g., [van der Kruit & Freeman 2011](#); [Gentile et al. 2013](#)), respectively, both of which are at least an order-of-magnitude smaller than the height of the modeled thick disk. On the other hand, H I observations of nearby edge-on galaxies found extra-planar H I gas several kpc or even ≈ 20 kpc from the disk midplane, e.g., NGC 891 ([Oosterloo et al. 2007](#)). These H I observations detect a lag in rotation speed as the distance from the disk plane increases, and some also measure a decrease in this vertical velocity gradient at the outer radii ([Oosterloo et al. 2007](#); [Zschaechner et al. 2012](#)). Multi-component models were developed to reproduce the measured H I column density distribution in different velocity bands, i.e., the H I channel maps. These models include some combinations of a thick disk with rotation lag, radial flow, flare, warps, and allow asymmetry between the approaching and receding sides of the rotation ([Oosterloo et al. 2007](#); [Zschaechner et al. 2012, 2015](#); [Kamphuis et al. 2013](#)). Is it possible that the Mg II gas structure resembles that of the H I gas but scaled up in size? Future work can explore this question by focusing on individual galaxies in zoom-in cosmological simulations and creating models to analyze the Mg II channel maps the same way as the H I channel maps in observational analyses.

5.3. Mg II Gas Distribution Around Quiescent Galaxies

The maps of the Mg II detection fraction (Figure 9) and the distribution of detectable corotating Mg II gas (Figure 13) potentially suggest that average quiescent galaxies have a more isotropic Mg II distribution and less “disky” morphologically and kinematically compared to their star-forming galaxy counterparts. While our re-

sults for quiescent galaxies may be subject to small number statistics (Table 2 and Section 4.1), the result that star-forming and quiescent galaxies have different Mg II gas properties is well supported by observational studies. For example, quiescent galaxies have a lower Mg II covering fraction than star-forming galaxies (Lan et al. 2014; Huang et al. 2020), and the covering fraction drops further for massive, luminous red galaxies (LRGs, Huang et al. 2016; Chen et al. 2018). Comparison of our Mg II detection maps between star-forming and quiescent galaxies agrees with this description, and plotting the detection fraction against impact parameter clearly demonstrates the lower detection rate for quiescent galaxies at a fixed impact parameter (Figure 15; thick curves). Also, strong Mg II systems are preferentially observed around star-forming galaxies, and the strength of the Mg II absorption shows an azimuthal dependence around star-forming galaxies but not around quiescent galaxies; the latter led to the conclusion that Mg II gas around quiescent galaxies is isotropically distributed (Bordoloi et al. 2011; Lan et al. 2014). These differences in the CGM between star-forming and quiescent galaxies are not limited to the low-ionization-state Mg II gas but also apply to the higher ions. For example, the highly ionized O^{+5} ion ubiquitously observed around $\sim L^*$ star-forming galaxies is rarely detected around quiescent galaxies in the COS-Halos survey (Tumlinson et al. 2011). While this dichotomy is reproduced by both the EAGLE (Oppenheimer et al. 2016) and IllustrisTNG simulations (Nelson et al. 2018), Oppenheimer et al. showed that the observed dichotomy largely reflects the higher halo mass of the quiescent galaxies compared to the star-forming galaxies in the COS-Halos sample, for which the O VI fraction peaks at the halo virial temperature of the $\sim L^*$ star-forming galaxies. Nevertheless, both EAGLE and IllustrisTNG predict that at a fixed halo mass, the CGM gas mass fraction strongly correlates with the galaxy sSFR (Davies et al. 2020). Hence, both observational and simulation studies have verified that star-forming and quiescent galaxies have different circumgalactic gas properties.

We also emphasize that our result of extended cool gas around quiescent galaxies (at least for those with $M_* \geq 10^{10} M_\odot$, Figure 9) is not surprising according to existing observational studies. Quasar absorption-line studies have measured a high incidence rate of metal enriched cool gas around quiescent galaxies (Thom et al. 2012; Werk et al. 2013; Huang et al. 2020) and massive LRGs (Gauthier et al. 2009; Huang et al. 2016; Chen et al. 2018; Berg et al. 2019; Zahedy et al. 2019), and the cool gas mass of LRGs is even comparable to that of $\sim L^*$ star-forming galaxies (Zahedy et al. 2019). Nelson

et al. (2020) recently used TNG50 to analyze the cool CGM around $z \sim 0.5$ massive galaxies analogous to the observed LRGs. They showed that the cool gas mass increases with halo mass, which again implies that LRGs and quiescent galaxies do not lack cool gas. They found that the cool gas takes the form of thousands of $\sim kpc$ -size, thermally underpressurized clouds dominated by magnetic pressure. This led to their conclusion that magnetic fields possibly influence the formation and the morphology of individual clouds of the cool CGM.

It is also worth noting that while our result suggests that the Mg II gas around quiescent galaxies is potentially less “disky” than that around their star-forming galaxy counterparts, it is not true that all of the simulated quiescent galaxies lack a rotating Mg II gas structure. A few of them have “disky” Mg II gas, even though this is less common compared to star-forming galaxies. While a “disky” gas structure may naively be unexpected for quiescent galaxies, especially because the majority of quiescent galaxies are elliptical and lenticular galaxies (Hubble 1936; Bernardi et al. 2010), a recent observational work studied local quiescent galaxies and found a surprising large reservoir of cold, rotating H I gas similar to that around star-forming galaxies (Zhang et al. 2019). These authors suggested that the galaxies are quenched not because of the lack of gas in general, but because of the reduced molecular gas content, lower star formation efficiency, and/or lower dust content compared to the star-forming galaxies.

5.4. Is there a cutoff radius for the Mg II gas to be observationally detected?

For both star-forming and quiescent galaxies, the Mg II detection fraction maps clearly indicate that the Mg II gas around higher mass galaxies has a larger physical extent (i.e., in pkpc). Comparing the detection fraction contours with the dashed circles representing $0.5r_{\text{vir}}$ (Figures 7 and 9) still shows that higher mass galaxies have a more extended Mg II gas distribution relative to the halo size, but the difference is less drastic; also see the Appendix, where we show the detection maps with pixels scaled with r_{vir} . This implies that the Mg II gas distribution around massive galaxies is intrinsically more extended.

Observational work has also demonstrated that the Mg II gas distribution depends on the mass and size of the host galaxy or halo. Quasar absorption-line studies often find that the strength of the Mg II absorption system (measured by the equivalent width (EW)) decreases with increasing impact parameter b of the quasar sightline, but the data points around this relation show a large scatter (Chen et al. 2010; Nielsen et al. 2013a;

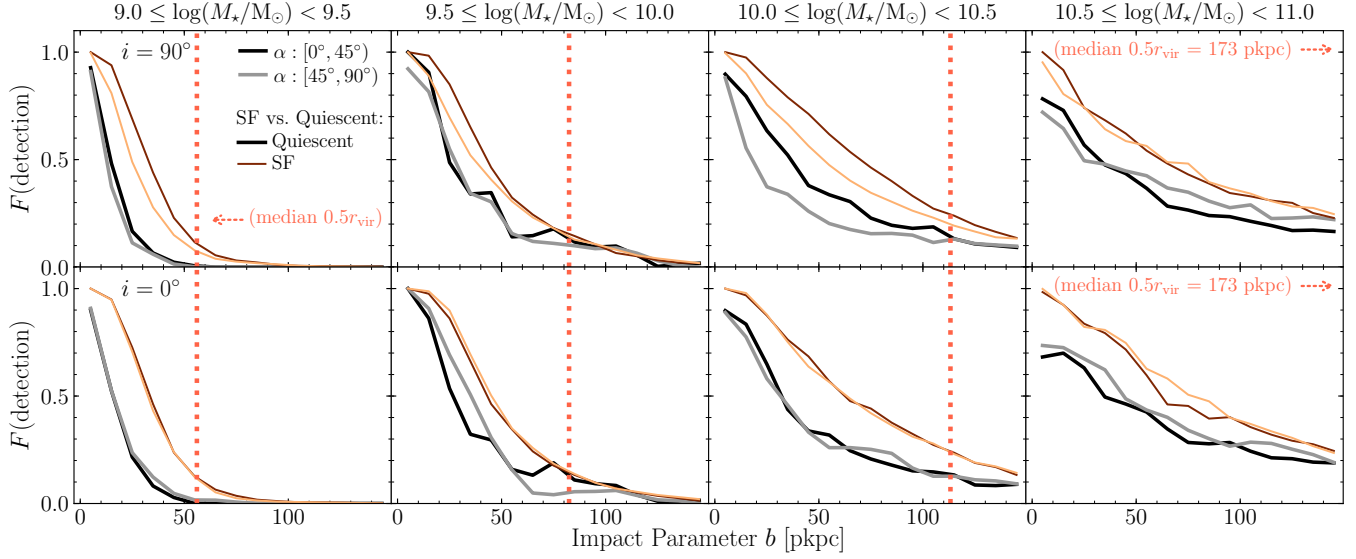


Figure 15. Mg II detection fraction as a function of impact parameter b for quiescent and star-forming galaxies projected at $i = 90^\circ$ (i.e., seen edge-on, top row) and 0° (i.e., seen face-on, bottom row). The solid curves represent the detection fractions obtained from gas physically within r_{vir} of quiescent (thick, greyish) and star-forming (thin, reddish) galaxies. Similar to Figure 10, different columns show the results for different stellar mass bins, and the darker (lighter) curve represents the azimuthal angle α range of $0^\circ \leq \alpha < 45^\circ$ ($45^\circ \leq \alpha < 90^\circ$), i.e., closer to the galaxy major (minor) axes. The vertical thick, dotted line in light red shows the median $0.5r_{\text{vir}}$ of the quiescent galaxies in the stack.

Huang et al. 2020). A mass segregation is also observed in the EW- b relation; at large impact parameters, the Mg II systems are detected around galaxies with higher masses (Churchill et al. 2013a). On the other hand, plotting Mg II EW vs. b/r_{vir} reduces the scatter compared to that of EW vs. b and improves the statistical significance of the fit (Churchill et al. 2013b; Huang et al. 2020), and plotting against $(b/r_{\text{vir}})^2$ removes the mass segregation (Churchill et al. 2013a,b). These results suggest that the circumgalactic Mg II gas distribution scales with halo mass and radius, and Churchill et al. also find that the majority of the Mg II gas resides within $b \lesssim 0.3r_{\text{vir}}$. The mass segregation observed matches with our result that Mg II gas is more extended around higher mass galaxies. However, the Mg II gas around the EAGLE galaxies extends beyond $0.3r_{\text{vir}}$. As seen from the Mg II detection maps in Figures 7 and A.1, although most of the detectable Mg II around $\log(M_*/M_\odot) < 10$ galaxies lies within $0.3r_{\text{vir}}$, for $\log(M_*/M_\odot) \geq 10$ galaxies, the 50% detection fraction extends further than $0.3r_{\text{vir}}$.

The extended Mg II distribution around EAGLE galaxies of higher mass also explains the trend of the Mg II mis-assignment fraction in Section 3. At a fixed impact parameter, the Mg II mis-assignment fraction is higher for a less massive galaxy compared to that for a more massive galaxy, implying that the Mg II gas selected by the $|\Delta v_{\text{LOS}}| = 500 \text{ km s}^{-1}$ window is more likely to lie outside of r_{vir} of the lower mass galaxy. This can be naturally explained by Mg II spatial ex-

tent scaling with halo size, because a fixed impact parameter in pkpc represents a larger fraction relative to the halo size for a lower mass galaxy. In fact, instead of selecting the Mg II gas within a fixed velocity window of $|\Delta v_{\text{LOS}}| = 500 \text{ km s}^{-1}$, we have explored using a window that scales with the halo mass and size and then recalculated the Mg II mis-assignment fraction. We used $|\Delta v_{\text{LOS}}| = 2v_{\text{c,halo}}$, where $v_{\text{c,halo}}$ represents the halo circular speed $v_{\text{c,halo}} = \sqrt{GM_{\text{vir}}/r_{\text{vir}}}$.⁹ Comparing the recalculated Mg II mis-assignment fractions to those with $|\Delta v_{\text{LOS}}| = 500 \text{ km s}^{-1}$ shows negligible differences for the galaxies in mass bins of $\log(M_*/M_\odot) \geq 10$, whereas those in $9 \leq \log(M_*/M_\odot) < 9.5$ ($9.5 \leq \log(M_*/M_\odot) < 10$) show a percentage decrease of $\lesssim 35\%$ (20%) relative to the original results obtained from the $\pm 500 \text{ km s}^{-1}$ window. This is not surprising, because $2v_{\text{c,halo}}$ of a lower mass galaxy covers a smaller velocity range than the fixed 500 km s^{-1} window. While this seems to suggest that observational studies should use a scalable window while associating the Mg II gas with target galaxies, neither r_{vir} nor M_{vir} are measured directly from observations.

5.5. Identifying circumgalactic gas around galaxies: where does the CGM end?

⁹ We apply the multiplicative factor of two such that $|\Delta v_{\text{LOS}}| \approx 500 \text{ km s}^{-1}$ for a $M_{\text{vir}} \approx 10^{12} M_\odot$ galaxy.

The CGM has been defined as the gas roughly within r_{vir} and outside of the interstellar medium of galaxies (e.g., Tumlinson et al. 2017). Many observations of the CGM have been conducted through quasar absorption-line studies, but associating the absorption system with a host galaxy and determining whether the absorbing gas is circumgalactic is not straightforward. First, observers do not know where the absorbing gas lies along the sightline in 3D-space. Second, the r_{vir} (and M_{vir}) of observed galaxies is highly uncertain. Typically, determining the r_{vir} of an observed galaxy requires the galaxy stellar mass (deduced from galaxy photometry) and the stellar mass-halo mass relation, which is model-dependent and has a large intrinsic scatter (e.g., Behroozi et al. 2013). As a result, observations typically associate an absorption system with a host galaxy if it is at a small projected separation from the quasar sightline and has a similar redshift as the absorption system. The latter is typically defined using a fixed LOS velocity window (e.g., $|\Delta v_{\text{LOS}}| = 500 \text{ km s}^{-1}$, Section 3).

Where the CGM ends is a topic of ongoing discussion (Shull 2014). If we assume r_{vir} sets the boundary of the CGM, then the Mg II mis-assignment fraction in Figure 4 shows how often the Mg II gas detected at a certain impact parameter comes from gas outside of r_{vir} but is selected by the $|\Delta v_{\text{LOS}}| \leq 500 \text{ km s}^{-1}$ criterion. This rate of mis-assignment is significant. For example, for a sightline at an impact parameter of 100 kpc, 80% (6%) of the times Mg II is mis-assigned for a galaxy with $9 \leq \log(M_*/M_\odot) < 9.5$ ($10 \leq \log(M_*/M_\odot) < 10.5$). This raises a warning flag for observational studies of the CGM, because observers often select gas around galaxies using the $|\Delta v_{\text{LOS}}|$ window. The mis-assigned Mg II gas contaminates the corotation signal and leads observers to underestimate the spatial extent of the corotating gas (Section 5.1). This also implies that the mis-assigned gas affects the study of gas kinematics in general, including the Doppler shift and the velocity spread measured in quasar sightlines. The mis-assigned gas may increase the width of the existing velocity component or create additional velocity components, depending on the velocity difference of gas inside (if detected) and outside of r_{vir} and the spectral resolution of the absorption spectra.

Ultimately, the issue of “mis-assigning” the host galaxy of the detected Mg II gas, or circumgalactic gas in general, originates from the question of what defines the CGM. For example, whether the CGM should be defined using a spatial boundary, e.g., a sphere with radius r_{vir} , or perhaps defined by the gas kinematics, e.g., the gas should be bound or selected using a velocity window. How to define the CGM can also depend on the objective of the study. For example, the r_{vir} boundary

is sufficient for studying the angular momentum of the cool CGM and how it grows the disk, because the disk-CGM interface lies well within r_{vir} . But to understand gas recycling and the chemical evolution of the CGM, it is necessary to include gas outside of r_{vir} , because this gas will eventually be (re-)accreted and change the metal content of the CGM. In any case, it is important to realize the potential bias of using any criterion of defining the extent of the CGM, associating absorption systems with target galaxies while studying the circumgalactic gas properties, and comparing results from observational measurements with those from cosmological simulations. Note that zoom-in cosmological simulations may not even model a volume sufficiently large to cover all the mis-assigned gas that falls within the velocity window.

6. CONCLUSION

Mg II gas has been widely studied in circumgalactic observations to characterize the properties of the cool, $\sim 10^4 \text{ K}$ CGM. In this paper, we used the high-resolution EAGLE (25 Mpc)³ cosmological simulation to analyze the Mg II gas around $z \approx 0.25$ galaxies. We focused on the Mg II morphological and rotation structures and examined how they vary with galaxy properties. Because observers often select the Mg II gas around target galaxies using a LOS velocity cut, we explored how often a LOS velocity window of $|\Delta v_{\text{LOS}}| = 500 \text{ km s}^{-1}$ selects Mg II gas outside of r_{vir} of the target galaxy. We discussed how this mis-assigned Mg II gas affects circumgalactic Mg II gas analyses in sightline studies.

We found that the Mg II gas around star-forming galaxies neither has a spherical distribution nor resides in a thin disk but has an axisymmetric structure. Over half of the galaxies have detectable rotating Mg II gas 20 pkpc from the midplane. The picture of an axisymmetric rotating structure also explains the azimuthal dependence of the corotating Mg II gas detection. The corotating gas is less frequently detected near the projected galaxy minor axes, which can be explained by winds and accretion from preferred directions. A similar rotating structure is less commonly found in our small sample of simulated quiescent galaxies. This potentially suggests that the Mg II distribution around quiescent galaxies is generally less “disky” and more isotropic. Nevertheless, for both star-forming and quiescent galaxies, the Mg II gas is more extended around galaxies with higher masses, both in terms of the physical size (in pkpc) and relative to the halo virial radius.

The picture of an axisymmetric rotating Mg II structure around star-forming galaxies provides support to

the interpretation of the circumgalactic absorption observed in quasar sightlines. These observations detected Mg II gas that corotates with the galaxy disks, but reproducing the broad Mg II linewidth required a rotating structures of tens of kiloparsec thick instead of a thin disk (Steidel et al. 2002; Kacprzak et al. 2010, 2011; Ho et al. 2017; Ho & Martin 2020). Our results demonstrate that thick Mg II rotating structures exists, which plausibly represents the Mg II gas structure probed by the quasar sightlines that detected Mg II corotation. Our description of the axisymmetric rotating Mg II gas also agrees with the recent *IllustrisTNG* simulation result of a circumgalactic angular momentum study, which suggested a cylindrically symmetric CGM (DeFelippis et al. 2020). We also noted that there exist nearby disks with H I extra-planar gas rotating and extending 20 kpc from the disk midplane. A future project can use simulations to examine whether the Mg II gas resembles a scaled-up H I gas structure and use multi-component disk models to analyze the Mg II gas in the same way as observational studies analyze the H I gas.

Since circumgalactic absorption studies often use a LOS velocity cut to select gas associated with galaxies, we explored how often adopting a $\pm 500 \text{ km s}^{-1}$ LOS velocity cut includes Mg II gas physically outside of r_{vir} , i.e., mis-assigned Mg II gas. We characterized the Mg II mis-assignment fraction as a function of impact parameter around host galaxies of different properties (Figure 4), and Table 3 provides the fitted parameters for the analytical function describing the relation. This provides an estimate for observers of how likely it is that the Mg II gas detected in a sightline actually comes from outside of r_{vir} of the target galaxy with known stellar mass. For example, at an impact parameter of 100 pkpc, the $\pm 500 \text{ km s}^{-1}$ velocity cut around galaxies with stellar masses of 10^9 - $10^{9.5} M_{\odot}$ (10^{10} - $10^{10.5} M_{\odot}$) selects detectable Mg II gas beyond r_{vir} 80% (6%) of the time. It would also be interesting to characterize this Mg II

mis-assignment issue using other cosmological simulations and compare with our results, so that observers can be better informed regarding how this issue affects their circumgalactic measurements. In particular, we demonstrated, according to our simulation, that not only does the mis-assigned Mg II gas increase the Mg II detection fraction especially at large impact parameters ($\gtrsim 80 \text{ pkpc}$), the mis-assigned Mg II gas also reduces the frequency of detecting corotating Mg II gas at impact parameters $\gtrsim 0.25r_{\text{vir}}$. This will lead observers to deduce a smaller extent for the corotating gas structure. Hence, the issue with the mis-assigned Mg II gas raises potential concerns regarding the interpretations of the circumgalactic gas measurements. It is important to realize the potential bias of using different methods to identify the circumgalactic gas around galaxies and comparing results from observations and cosmological simulations.

We thank the referee for comments that improved the manuscript. We thank Max Gronke, Kim-Vy Tran, and Anshu Gupta for insightful discussions and comments that improved this work. We also thank Peter Mitchell, Nastasha Wijers, and Sylvia Ploekinger for the early discussions on this work, and we greatly appreciate their technical support with implementing the ionization tables and testing the code of making projection maps. This work is partially supported by the National Science Foundation under AST-1817125. This work used the DiRAC@Durham facility managed by the Institute for Computational Cosmology on behalf of the STFC DiRAC HPC Facility (www.dirac.ac.uk). The equipment was funded by BEIS capital funding via STFC capital grants ST/K00042X/1, ST/P002293/1, ST/R002371/1 and ST/S002502/1, Durham University and STFC operations grant ST/R000832/1. DiRAC is part of the National e-Infrastructure.

REFERENCES

- Bahé, Y. M., Crain, R. A., Kauffmann, G., et al. 2016, *MNRAS*, 456, 1115
- Behroozi, P. S., Wechsler, R. H., & Conroy, C. 2013, *ApJ*, 770, 57
- Berg, M. A., Howk, J. C., Lehner, N., et al. 2019, *ApJ*, 883, 5
- Bernardi, M., Shankar, F., Hyde, J. B., et al. 2010, *MNRAS*, 404, 2087
- Bordoloi, R., Lilly, S. J., Knobel, C., et al. 2011, *ApJ*, 743, 10
- Borisova, E., Cantalupo, S., Lilly, S. J., et al. 2016, *ApJ*, 831, 39
- Borthakur, S., Heckman, T., Tumlinson, J., et al. 2015, *ApJ*, 813, 46
- . 2016, *ApJ*, 833, 259
- Bouché, N., Hohensee, W., Vargas, R., et al. 2012, *MNRAS*, 426, 801
- Bouché, N., Murphy, M. T., Kacprzak, G. G., et al. 2013, *Science*, 341, 50
- Bouché, N., Finley, H., Schroetter, I., et al. 2016, *ApJ*, 820, 121

- Bowen, D. V., Chelouche, D., Jenkins, E. B., et al. 2016, *ApJ*, 826, 50
- Bryan, G. L., & Norman, M. L. 1998, *ApJ*, 495, 80
- Bryan, G. L., Norman, M. L., O’Shea, B. W., et al. 2014, *ApJS*, 211, 19
- Burchett, J. N., Rubin, K. H. R., Prochaska, J. X., et al. 2020, arXiv e-prints, arXiv:2005.03017
- Cai, Z., Cantalupo, S., Prochaska, J. X., et al. 2019, *ApJS*, 245, 23
- Cantalupo, S., Arrigoni-Battaia, F., Prochaska, J. X., Hennawi, J. F., & Madau, P. 2014, *Nature*, 506, 63
- Charlton, J. C., & Churchill, C. W. 1998, *ApJ*, 499, 181
- Chen, H.-W., Gauthier, J.-R., Sharon, K., et al. 2014, *MNRAS*, 438, 1435
- Chen, H.-W., Helsby, J. E., Gauthier, J.-R., et al. 2010, *ApJ*, 714, 1521
- Chen, H.-W., Zahedy, F. S., Johnson, S. D., et al. 2018, *MNRAS*, 479, 2547
- Chisholm, J., Prochaska, J. X., Schaerer, D., Gazagnes, S., & Henry, A. 2020, arXiv e-prints, arXiv:2008.06059
- Churchill, C. W., Nielsen, N. M., Kacprzak, G. G., & Trujillo-Gomez, S. 2013a, *ApJL*, 763, L42
- Churchill, C. W., Steidel, C. C., & Vogt, S. S. 1996, *ApJ*, 471, 164
- Churchill, C. W., Trujillo-Gomez, S., Nielsen, N. M., & Kacprzak, G. G. 2013b, *ApJ*, 779, 87
- Correa, C. A., Schaye, J., van de Voort, F., Duffy, A. R., & Wyithe, J. S. B. 2018a, *MNRAS*, 478, 255
- Correa, C. A., Schaye, J., Wyithe, J. S. B., et al. 2018b, *MNRAS*, 473, 538
- Crain, R. A., Schaye, J., Bower, R. G., et al. 2015, *MNRAS*, 450, 1937
- Crain, R. A., Bahé, Y. M., Lagos, C. d. P., et al. 2017, *MNRAS*, 464, 4204
- Danovich, M., Dekel, A., Hahn, O., Ceverino, D., & Primack, J. 2015, *MNRAS*, 449, 2087
- Davies, J. J., Crain, R. A., Oppenheimer, B. D., & Schaye, J. 2020, *MNRAS*, 491, 4462
- de Grijs, R. 1998, *MNRAS*, 299, 595
- De Young, D. S., & Heckman, T. M. 1994, *ApJ*, 431, 598
- DeFelippis, D., Genel, S., Bryan, G. L., et al. 2020, *ApJ*, 895, 17
- Dekel, A., Birnboim, Y., Engel, G., et al. 2009, *Nature*, 457, 451
- Diamond-Stanic, A. M., Coil, A. L., Moustakas, J., et al. 2016, *ApJ*, 824, 24
- Dolag, K., Borgani, S., Murante, G., & Springel, V. 2009, *MNRAS*, 399, 497
- El-Badry, K., Quataert, E., Wetzel, A., et al. 2018, *MNRAS*, 473, 1930
- Faucher-Giguère, C.-A. 2020, *MNRAS*, 493, 1614
- Ferland, G. J., Chatzikos, M., Guzmán, F., et al. 2017, *RMxAA*, 53, 385
- Ford, A. B., Davé, R., Oppenheimer, B. D., et al. 2014, *MNRAS*, 444, 1260
- Ford, A. B., Werk, J. K., Davé, R., et al. 2016, *MNRAS*, 459, 1745
- French, D. M., & Wakker, B. P. 2020, *ApJ*, 897, 151
- Furlong, M., Bower, R. G., Theuns, T., et al. 2015, *MNRAS*, 450, 4486
- Furlong, M., Bower, R. G., Crain, R. A., et al. 2017, *MNRAS*, 465, 722
- Gauthier, J.-R., Chen, H.-W., & Tinker, J. L. 2009, *ApJ*, 702, 50
- Gentile, G., Józsa, G. I. G., Serra, P., et al. 2013, *A&A*, 554, A125
- Gronke, M., & Oh, S. P. 2020, *MNRAS*, 492, 1970
- Guo, Y., Maiolino, R., Jiang, L., et al. 2020, *ApJ*, 898, 26
- Gutcke, T. A., Stinson, G. S., Macciò, A. V., Wang, L., & Dutton, A. A. 2017, *MNRAS*, 464, 2796
- Hafen, Z., Faucher-Giguere, C.-A., Angles-Alcazar, D., et al. 2018, arXiv e-prints, arXiv:1811.11753
- Heckman, T., Borthakur, S., Wild, V., Schiminovich, D., & Bordoloi, R. 2017, *ApJ*, 846, 151
- Ho, S. H., & Martin, C. L. 2020, *ApJ*, 888, 14
- Ho, S. H., Martin, C. L., Kacprzak, G. G., & Churchill, C. W. 2017, *ApJ*, 835, 267
- Ho, S. H., Martin, C. L., & Turner, M. L. 2019, *ApJ*, 875, 54
- Huang, Y.-H., Chen, H.-W., Johnson, S. D., & Weiner, B. J. 2016, *MNRAS*, 455, 1713
- Huang, Y.-H., Chen, H.-W., Shectman, S. A., et al. 2020, arXiv e-prints, arXiv:2009.12372
- Hubble, E. P. 1936, *Realm of the Nebulae*
- Hummels, C. B., Bryan, G. L., Smith, B. D., & Turk, M. J. 2013, *MNRAS*, 430, 1548
- Hummels, C. B., Smith, B. D., Hopkins, P. F., et al. 2019, *ApJ*, 882, 156
- Huscher, E., Oppenheimer, B. D., Lonardi, A., et al. 2020, arXiv e-prints, arXiv:2005.06310
- Kacprzak, G. G., Churchill, C. W., Barton, E. J., & Cooke, J. 2011, *ApJ*, 733, 105
- Kacprzak, G. G., Churchill, C. W., Ceverino, D., et al. 2010, *ApJ*, 711, 533
- Kacprzak, G. G., Churchill, C. W., & Nielsen, N. M. 2012, *ApJL*, 760, L7
- Kacprzak, G. G., Churchill, C. W., Steidel, C. C., Murphy, M. T., & Evans, J. L. 2007, *ApJ*, 662, 909
- Kacprzak, G. G., Muzahid, S., Churchill, C. W., Nielsen, N. M., & Charlton, J. C. 2015, *ApJ*, 815, 22

- Kacprzak, G. G., Vander Vliet, J. R., Nielsen, N. M., et al. 2019, *ApJ*, 870, 137
- Kamphuis, P., Rand, R. J., Józsa, G. I. G., et al. 2013, *MNRAS*, 434, 2069
- Kauffmann, G., Borthakur, S., & Nelson, D. 2016, *MNRAS*, 462, 3751
- Kauffmann, G., Nelson, D., Borthakur, S., et al. 2019, *MNRAS*, 486, 4686
- Kulkarni, V. P., Cashman, F. H., Lopez, S., et al. 2019, *ApJ*, 886, 83
- Lagos, C. d. P., Crain, R. A., Schaye, J., et al. 2015, *MNRAS*, 452, 3815
- Lan, T.-W., Ménard, B., & Zhu, G. 2014, *ApJ*, 795, 31
- Lan, T.-W., & Mo, H. 2018, *ApJ*, 866, 36
- Lanzetta, K. M., & Bowen, D. V. 1992, *ApJ*, 391, 48
- Leclercq, F., Bacon, R., Wisotzki, L., et al. 2017, *A&A*, 608, A8
- Liang, C. J., Kravtsov, A. V., & Agertz, O. 2016, *MNRAS*, 458, 1164
- Lopez, S., Tejos, N., Ledoux, C., et al. 2018, *Nature*, 554, 493
- Lopez, S., Tejos, N., Barrientos, L. F., et al. 2019, *MNRAS*, 2763
- Martin, C. L., Ho, S. H., Kacprzak, G. G., & Churchill, C. W. 2019, *ApJ*, 878, 84
- McAlpine, S., Helly, J. C., Schaller, M., et al. 2016, *Astronomy and Computing*, 15, 72
- Mitchell, P. D., Schaye, J., Bower, R. G., & Crain, R. A. 2020, *MNRAS*, 494, 3971
- Morrissey, P., Matuszewski, M., Martin, D. C., et al. 2018, *ApJ*, 864, 93
- Moustakas, J., Coil, A. L., Aird, J., et al. 2013, *ApJ*, 767, 50
- Muzahid, S. 2014, *ApJ*, 784, 5
- Nelson, D., Kauffmann, G., Pillepich, A., et al. 2018, *MNRAS*, 477, 450
- Nelson, D., Sharma, P., Pillepich, A., et al. 2020, *arXiv e-prints*, arXiv:2005.09654
- Nielsen, N. M., Churchill, C. W., & Kacprzak, G. G. 2013a, *ApJ*, 776, 115
- Nielsen, N. M., Churchill, C. W., Kacprzak, G. G., & Murphy, M. T. 2013b, *ApJ*, 776, 114
- Nielsen, N. M., Churchill, C. W., Kacprzak, G. G., Murphy, M. T., & Evans, J. L. 2015, *ApJ*, 812, 83
- Nielsen, N. M., Kacprzak, G. G., Muzahid, S., et al. 2017, *ApJ*, 834, 148
- Oosterloo, T., Fraternali, F., & Sancisi, R. 2007, *AJ*, 134, 1019
- Oppenheimer, B. D. 2018, *MNRAS*, 480, 2963
- Oppenheimer, B. D., & Schaye, J. 2013, *MNRAS*, 434, 1063
- Oppenheimer, B. D., Schaye, J., Crain, R. A., Werk, J. K., & Richings, A. J. 2018a, *MNRAS*, 481, 835
- Oppenheimer, B. D., Segers, M., Schaye, J., Richings, A. J., & Crain, R. A. 2018b, *MNRAS*, 474, 4740
- Oppenheimer, B. D., Crain, R. A., Schaye, J., et al. 2016, *MNRAS*, 460, 2157
- Peebles, M. S., Corlies, L., Tumlinson, J., et al. 2019, *ApJ*, 873, 129
- Péroux, C., Rahmani, H., Arrigoni Battaia, F., & Augustin, R. 2018, *MNRAS*, 479, L50
- Planck Collaboration, Ade, P. A. R., Aghanim, N., et al. 2014, *A&A*, 571, A16
- Ploekinger, S., & Schaye, J. 2020, *MNRAS*, doi:10.1093/mnras/staa2172
- Prochaska, J. X., & Wolfe, A. M. 1997, *ApJ*, 487, 73
- Rahmati, A., Schaye, J., Bower, R. G., et al. 2015, *MNRAS*, 452, 2034
- Rahmati, A., Schaye, J., Crain, R. A., et al. 2016, *MNRAS*, 459, 310
- Rakic, O., Schaye, J., Steidel, C. C., & Rudie, G. C. 2012, *ApJ*, 751, 94
- Rubin, K. H. R., Diamond-Stanic, A. M., Coil, A. L., Crighton, N. H. M., & Moustakas, J. 2018a, *ApJ*, 853, 95
- Rubin, K. H. R., O’Meara, J. M., Cooksey, K. L., et al. 2018b, *ApJ*, 859, 146
- Schaller, M., Dalla Vecchia, C., Schaye, J., et al. 2015, *MNRAS*, 454, 2277
- Schaye, J., & Dalla Vecchia, C. 2008, *MNRAS*, 383, 1210
- Schaye, J., Crain, R. A., Bower, R. G., et al. 2015, *MNRAS*, 446, 521
- Schneider, E. E., Robertson, B. E., & Thompson, T. A. 2018, *ApJ*, 862, 56
- Schroetter, I., Bouché, N. F., Zabl, J., et al. 2019, *MNRAS*, 490, 4368
- Segers, M. C., Crain, R. A., Schaye, J., et al. 2016, *MNRAS*, 456, 1235
- Shao, S., Cautun, M., Frenk, C. S., et al. 2018, *MNRAS*, 476, 1796
- Shull, J. M. 2014, *ApJ*, 784, 142
- Springel, V. 2005, *MNRAS*, 364, 1105
- . 2010, *MNRAS*, 401, 791
- Springel, V., White, S. D. M., Tormen, G., & Kauffmann, G. 2001, *MNRAS*, 328, 726
- Steidel, C. C., Kollmeier, J. A., Shapley, A. E., et al. 2002, *ApJ*, 570, 526
- Stevens, A. R. H., Lagos, C. d. P., Contreras, S., et al. 2017, *MNRAS*, 467, 2066
- Stewart, K. R., Brooks, A. M., Bullock, J. S., et al. 2013, *ApJ*, 769, 74

- Stewart, K. R., Kaufmann, T., Bullock, J. S., et al. 2011, *ApJ*, 738, 39
- Suresh, J., Rubin, K. H. R., Kannan, R., et al. 2017, *MNRAS*, 465, 2966
- Thom, C., Tumlinson, J., Werk, J. K., et al. 2012, *ApJL*, 758, L41
- Trayford, J. W., Theuns, T., Bower, R. G., et al. 2015, *MNRAS*, 452, 2879
- Trayford, J. W., Camps, P., Theuns, T., et al. 2017, *MNRAS*, 470, 771
- Tumlinson, J., Peebles, M. S., & Werk, J. K. 2017, *ARA&A*, 55, 389
- Tumlinson, J., Thom, C., Werk, J. K., et al. 2011, *Science*, 334, 948
- . 2013, *ApJ*, 777, 59
- Turner, M. L., Schaye, J., Crain, R. A., et al. 2017, *MNRAS*, 471, 690
- Turner, M. L., Schaye, J., Crain, R. A., Theuns, T., & Wendt, M. 2016, *MNRAS*, 462, 2440
- Turner, M. L., Schaye, J., Steidel, C. C., Rudie, G. C., & Strom, A. L. 2014, *MNRAS*, 445, 794
- van de Voort, F., & Schaye, J. 2012, *MNRAS*, 423, 2991
- van de Voort, F., Springel, V., Mandelker, N., van den Bosch, F. C., & Pakmor, R. 2019, *MNRAS*, 482, L85
- van der Kruit, P. C., & Freeman, K. C. 2011, *ARA&A*, 49, 301
- Werk, J. K., Prochaska, J. X., Thom, C., et al. 2013, *ApJS*, 204, 17
- Wiersma, R. P. C., Schaye, J., & Smith, B. D. 2009, *MNRAS*, 393, 99
- Wijers, N. A., Schaye, J., & Oppenheimer, B. D. 2020, arXiv e-prints, arXiv:2004.05171
- Wijers, N. A., Schaye, J., Oppenheimer, B. D., Crain, R. A., & Nicastro, F. 2019, *MNRAS*, 488, 2947
- Wisotzki, L., Bacon, R., Blaizot, J., et al. 2016, *A&A*, 587, A98
- Wisotzki, L., Bacon, R., Brinchmann, J., et al. 2018, *Nature*, 562, 229
- Zabl, J., Bouché, N. F., Schroetter, I., et al. 2019, *MNRAS*, 485, 1961
- . 2020, *MNRAS*, 492, 4576
- Zahedy, F. S., Chen, H.-W., Johnson, S. D., et al. 2019, *MNRAS*, 484, 2257
- Zahedy, F. S., Chen, H.-W., Rauch, M., Wilson, M. L., & Zabludoff, A. 2016, *MNRAS*, 458, 2423
- Zhang, C., Peng, Y., Ho, L. C., et al. 2019, *ApJL*, 884, L52
- Zhang, H., Zaritsky, D., & Behroozi, P. 2018, *ApJ*, 861, 34
- Zhang, H., Zaritsky, D., Zhu, G., Ménard, B., & Hogg, D. W. 2016, *ApJ*, 833, 276
- Zhu, G., Ménard, B., Bizyaev, D., et al. 2014, *MNRAS*, 439, 3139
- Zschaechner, L. K., Rand, R. J., Heald, G. H., Gentile, G., & Józsa, G. 2012, *ApJ*, 760, 37
- Zschaechner, L. K., Rand, R. J., & Walterbos, R. 2015, *ApJ*, 799, 61

APPENDIX

A. Mg II DETECTION FRACTION MAPS WITH PIXELS SCALED WITH r_{vir}

In Section 4.1, we explained that for higher mass galaxies, not only does the Mg II gas have a larger radial extent in terms of its physical size (i.e., in pkpc), but also relative to the halo size. Figure A.1 and A.2 show the Mg II detection fraction for star-forming and quiescent galaxies, respectively, projected at $i = 90^\circ$. Each pixel is scaled by r_{vir} of individual galaxies (Section 2.3). The Mg II gas around higher mass galaxies still extends to larger radii relative to r_{vir} compared to the lower mass galaxies. For example, for the star-forming galaxies, 50% of the $10 \leq \log(M_*/M_\odot) < 10.5$ galaxies “detect” Mg II gas out to $\approx 0.35r_{\text{vir}}$, in contrast to only $\approx 0.25r_{\text{vir}}$ for the $9 \leq \log(M_*/M_\odot) < 9.5$ galaxies.

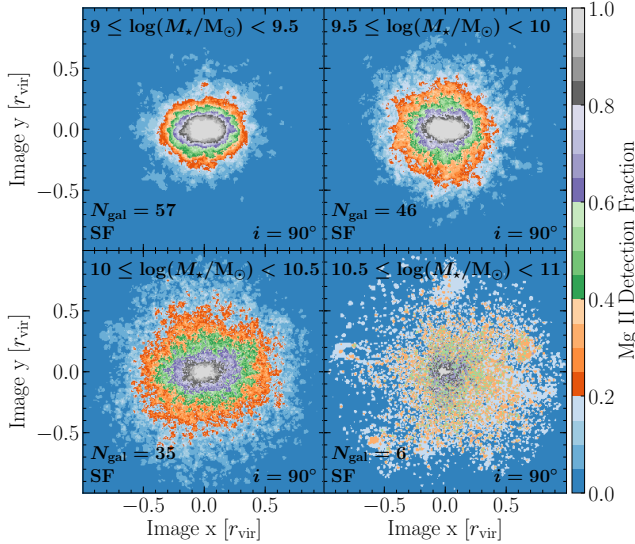


Figure A.1. Mg II detection fraction around star-forming galaxies with length parameters scaled by r_{vir} . The four panels show the stack of star-forming galaxies with different stellar masses (labeled at the top), and all galaxies are projected at $i = 90^\circ$. Compared to lower mass galaxies, the Mg II gas around higher mass galaxies extends to larger radii relative to r_{vir} .

B. Mg II DETECTION FRACTION FROM GAS SELECTED WITH $|\Delta v_{\text{LOS}}| \leq 500 \text{ km s}^{-1}$

Figure B.1 shows the Mg II detection fraction maps for $i = 90^\circ$ star-forming galaxies, for which the gas is selected to be within $|\Delta v_{\text{LOS}}| = 500 \text{ km s}^{-1}$ of the systemic velocities of individual galaxies. Comparing these maps with those calculated from the Mg II gas within

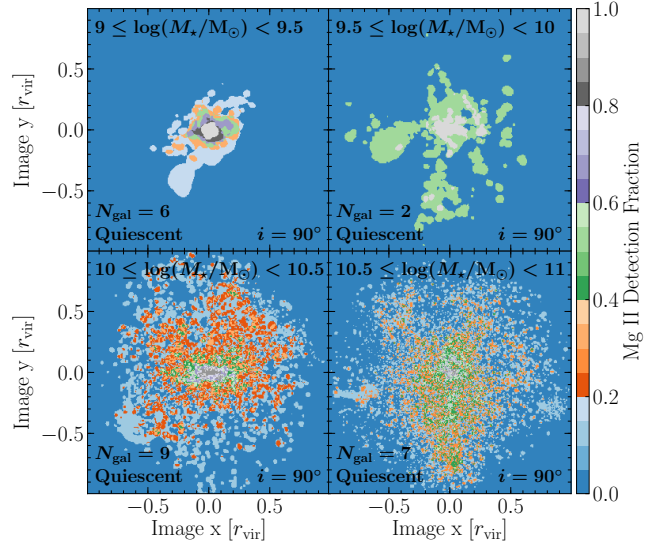


Figure A.2. Mg II detection fraction around quiescent galaxies with length parameters scaled by r_{vir} . The four panels have the same arrangement as those in Figure A.1.

r_{vir} (first row of Figure 7), the new light blue patches near the edge of the maps ($\gtrsim 0.5r_{\text{vir}}$) indicate an increase in the detection fraction from around 0 to $\lesssim 0.1$ if we select the Mg II gas by $|\Delta v_{\text{LOS}}| \leq 500 \text{ km s}^{-1}$.

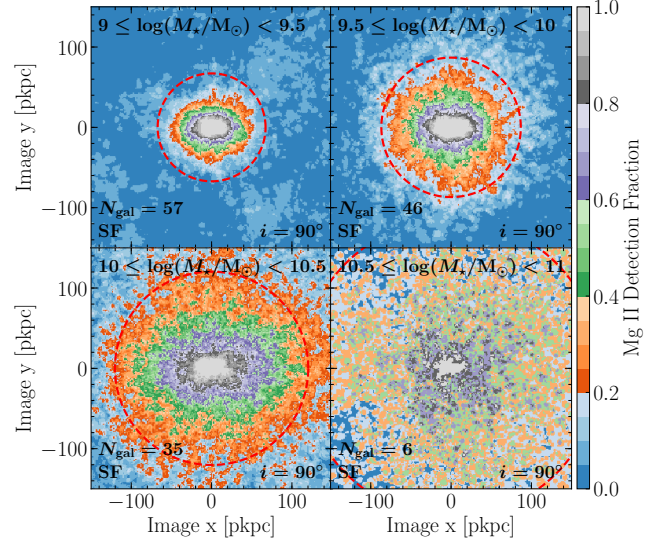


Figure B.1. Detection fraction of Mg II gas within $|\Delta v_{\text{LOS}}| = 500 \text{ km s}^{-1}$ from the systemic velocities of star-forming galaxies. All galaxies are projected at $i = 90^\circ$. This figure is similar to the first row of Figure 7, but instead of selecting the Mg II gas enclosed by r_{vir} , here we select the Mg II gas using the LOS velocity window $|\Delta v_{\text{LOS}}| = 500 \text{ km s}^{-1}$.